

# Data analysis in Turn-by-Turn BPMs signals of SuperKEKB main rings

---

**Andrés Gómez**

Master degree of Physics  
Erasmus Mundus LASCALA

Internship carried out at  
Laboratoire Interdisciplinaire des Sciences du Numérique

**Supervisor** Francesca Bugiotti  
**Co-supervisor** Barbara Dalena

25<sup>th</sup> August 2025

Orsay, France

## **Acknowledgments**

I would like to express my deepest gratitude to my supervisors, Francesca and Barbara, for their invaluable guidance, continuous support, and for believing in my abilities from the very beginning. Their trust, encouragement, and insightful advice have been instrumental in shaping both this work and my growth as a researcher.

I am also profoundly thankful to my family, whose unconditional love and constant encouragement have been my greatest source of inspiration. Their patience, and belief in me have given me the strength to persevere throughout this journey.

---

# Contents

---

<b>Abstract</b>	<b>1</b>	
<b>1</b>	<b>Introduction</b>	<b>2</b>
1.1	SuperKEKB Collider . . . . .	3
1.1.1	Beam Position Monitors . . . . .	4
1.1.2	Read-out electronics . . . . .	7
<b>2</b>	<b>Optics Concepts in Accelerator Physics</b>	<b>9</b>
2.1	Equation of motion . . . . .	10
2.2	Linear Transfer Map . . . . .	11
2.2.1	Drift Space . . . . .	11
2.2.2	Dipole Magnets . . . . .	11
2.2.3	Quadrupole Magnets . . . . .	12
2.3	Twiss Functions . . . . .	13
<b>3</b>	<b>Resonance Driving Terms</b>	<b>15</b>
3.1	Motivations . . . . .	15
3.2	Nonlinear Lattice . . . . .	17
3.2.1	One-turn map and nonlinearities . . . . .	17
3.2.2	Definition and Derivation of RDTs . . . . .	20
3.2.3	Frequency Spectrum . . . . .	22
3.2.4	Resonance classification and nomenclature . . . . .	23
<b>4</b>	<b>SOMA Package</b>	<b>26</b>

4.1	Raw data and Preprocessing . . . . .	26
4.2	Harmonic Analysis . . . . .	30
4.2.1	First Harmonic Analysis . . . . .	30
4.2.2	Synchronization . . . . .	30
4.2.3	Second Harmonic Analysis . . . . .	33
4.3	Optics Analysis . . . . .	35
4.3.1	RDTs . . . . .	37
<b>5</b>	<b>Tracking Analysis</b>	<b>41</b>
5.1	Tracking data . . . . .	41
5.2	Harmonic Analysis . . . . .	44
5.3	Optics Analysis . . . . .	45
5.3.1	RDTs . . . . .	47
5.4	Cross validation . . . . .	49
<b>Conclusions</b>		<b>54</b>
<b>Appendices</b>		<b>56</b>
A	BPM features . . . . .	56
B	Amplitude, Resonances and Lines . . . . .	59
C	Declaration of Originality . . . . .	62
<b>List of Figures</b>		<b>65</b>
<b>List of Tables</b>		<b>66</b>
<b>Bibliography</b>		<b>67</b>

---

# Abstract

---

This project involves the analysis of raw Beam Position Monitor (BPM) data from the SuperKEKB collider using the SOMA framework for signal processing and analysis. In parallel, the development of simulations for contrast with experimental data are covered. Key features such as beam centroid positions in both transverse planes ( $x$  and  $y$ ) are extracted, denoised via Singular Value Decomposition (SVD), and transformed into the frequency domain using Fast Fourier Transform (FFT). The resulting spectra reveal significant peaks corresponding to physical aspects of the SuperKEKB lattice, including synchrotron frequencies and possible lattice imperfections, which can be explained by the Resonance Driving Term formalism for high order multipole magnetic fields. The research aims to exploit data signals by SOMA's algorithms pipelines, search for nonlinearities until octupolar order, and processing tracking simulations for records of horizontal kicks in the beam. Tracking results present in general an agreement with the experimental data, with some specific misalignments, such as exceed in the octupolar contributions.

**Keywords:** Beam Position Monitor, Synchronization, Spectrum, Tracking, Optics, Resonance Driving Term.

---

# 1

---

# Introduction

---

---

Optics control in particle accelerators is a fundamental requirement in order to obtain high performance and operational stability in modern colliders such as SuperKEKB. As these machines operate closer to their design limits, the impact of higher-order multipolar magnetic field components becomes significant, demanding precise correction strategies to keep optimal beam conditions. Nonlinearities arising from magnetic field imperfections can reduce dynamic aperture, compromise beam stability, and shorten beam lifetime, making their mitigation a critical challenge for current and future accelerator projects.

The Large Hadron Collider (LHC) has been a key reference point for the development of advanced optics correction techniques. Computational tools and analysis methods created and developed for the LHC have proven highly effective for studying and compensating higher-order nonlinearities that affect beam quality. In this work, these LHC-developed codes and methodologies are adapted and applied to the SuperKEKB electron–positron collider, providing a unique opportunity to benchmark their performance in a low-emittance, high-luminosity environment.

The primary objective of this study is to explore beam-based techniques for the measurement of higher-order effects in SuperKEKB optics, exploring the advantages and results of SOMA, as well as its performance between experimental and simulation data. Successfully adapting and validating these techniques progressively not only benefits the immediate optimization of SuperKEKB but also advances the broader understanding of nonlinear dynamics in circular colliders, information to keep into account for the design and operation of next-generation high-luminosity machines.

The first two chapters of this work introduce the theoretical background of linear beam dy-

namics and optics together with the resonance driving terms (RDTs) formalism and the role they play in nonlinear optics. Chapter 4 describes the experimental data processing pipeline, including the use of the SOMA package, as one of the first developments of LHC tools for SuperKEKB. Description of different harmonic and optic analyses are presented, sketching the main results and quantities. Finally, chapter 5 develops a similar pipeline of processing employing simulated beam optics data, achieved from SuperKEKB software, with the goal to contrast experimental and simulation optics functions. Finally, conclusions for these studies are drawn at the end of this work.

## 1.1. SuperKEKB Collider

SuperKEKB is an asymmetric-energy electron-positron double-ring collider constructed by upgrading the KEKB previous B-Factory, which operated from 1998 until June 2010, achieved the worlds highest luminosity ( $2.11 \cdot 10^{34} \text{ cm}^{-2} \text{s}^{-1}$ ). Using these data, the Belle collaboration succeeded in proving the Kobayashi-Maskawa theory and obtained a variety of important experimental results in elementary particle physics. Based on the success of KEKB, upgrading to SuperKEKB, which significantly pushes the luminosity frontier toward more detailed experiments that seek new physics beyond the Standard Model, is considered an urgent issue in elementary particle physics [1].

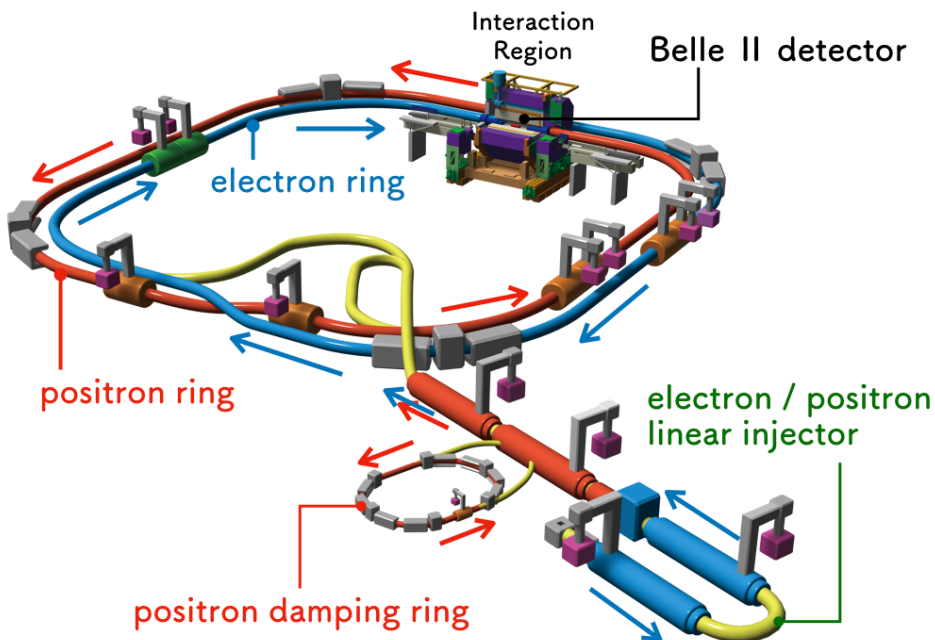


Figure 1.1: Schematic drawing of the accelerator complex at KEK [2].

The SuperKEKB collider complex consists of a 7-GeV electron ring (the high-energy ring, HER), a 4-GeV positron ring (the low-energy ring, LER) as shown in Figure 1.2, and an injector linear accelerator (linac) with a 1.1-GeV positron damping ring (DR), presented in Figure 1.1. To reach the extremely high luminosity of SuperKEKB required significant upgrades to the HER, LER, and final-focus system of KEKB. The injector linac also required significant upgrades for injection beams with high current and low emittance, as well as for improving simultaneous top-up injections. A new DR was designed and constructed for low-emittance positron beam injection [1]. Main upgrades in KEKB include the new final-focus superconducting magnets (quadrupoles and correctors), installation of Belle-II detector, renovation of diagnostics and control systems at the interaction region, and construction of the damping ring.

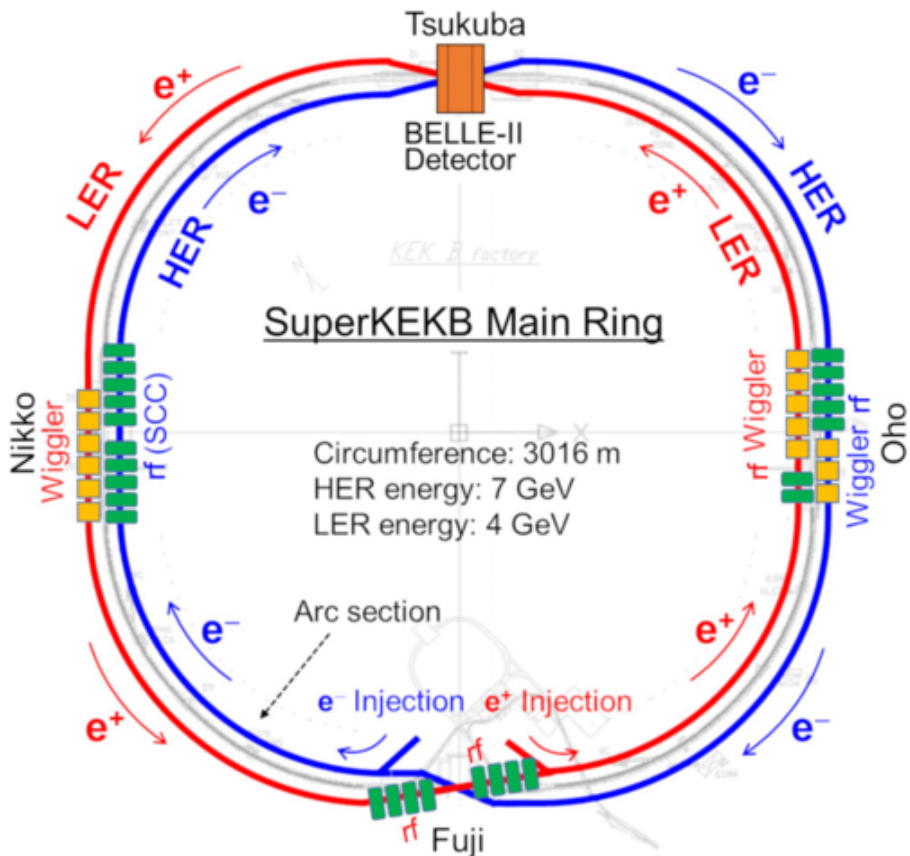


Figure 1.2: Layout of the SuperKEKB Main Ring (MR). One ring consists of four arc sections, four straight sections, and one collision point at Tsukuba (Belle II) [3].

### 1.1.1. Beam Position Monitors

The beam position monitor (BPM) system is one of the most utilized and powerful beam instrumentation tools in a particle accelerator or accelerator beam-line. A BPM system consists out of many beam position monitors distributed along the accelerator beam-line, monitoring

the passing beam. Each beam position monitor consists first of a non-invasive BPM pickup which is part of the vacuum chamber and consists out of two or four symmetrically arranged electrodes which couple to the electromagnetic fields of the beam and generate electrical signals at their output ports. The second is the read-out electronics, which is used to condition and process the signals from the pickup electrodes to provide the beam position information in a digital data format, so that it can be acquired and further processed by the accelerator control system. Popular BPM pickup styles are of button or stripline type, have broadband characteristics, and generate a pulse-like output signal for each passing bunch. This enables Turn-by-Turn BPM signal processing possibilities, but requires the synchronization of the BPM data of all monitors in the system. In a ring accelerator a synchronized Turn-by-Turn monitoring of the beam position is of interest to follow the response of the beam to a kick or chirp excitation, e.g. for beam optics studies and analysis. Averaging the BPM data over many turns (ring accelerator) or over many beam pulses (linac) at each BPM provides a high resolution measurement of the beam orbit or beam trajectory, used for the alignment of the beam, for an orbit feedback, etc.[4].

The main rings of SuperKEKB have about 900 quadrupole magnets, with one BPM of four electrodes (see Figure 1.3) associated to each quadrupole for precise orbit control. From that quantity of monitors, 68 in HER and 70 in LER can be used for Turn-by-Turn measurements (either the full list of BPMs names as technical features can be found in appendix A), employing a trigger system which starts data acquisition automatically when the beam is excited, usually by a Injection Kicker, for around 4600 to 5300 turns [5].

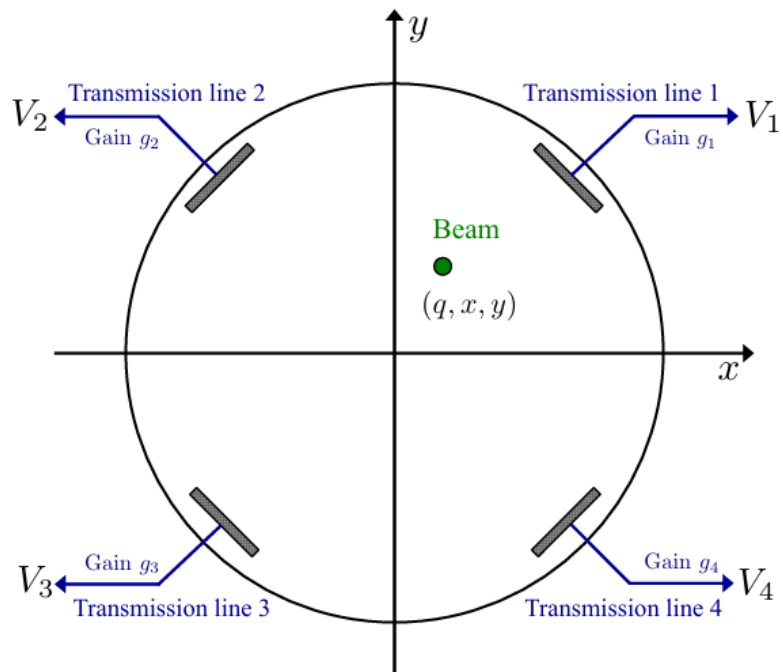


Figure 1.3: Schematic view of the BPM model used in SuperKEKB [6].



Figure 1.4: BPM pickups used for HER (left) of 12 mm and for LER (right) of 6 mm [7].

As the prior Figure, BPMs principal structure includes four metallic electrode, which are positioned symmetrically along the horizontal and vertical axes within a circular cross-section vacuum chamber. The horizontal ( $x$ ) and vertical ( $y$ ) offsets of the beam trajectory with respect to the chamber center define the beam position (or displacement). This position must be monitored with high resolution, accuracy, and repeatability, which constitutes the primary objective of beam position measurement [4]. They operate on the principle of image currents or image charges, each charged particle induces an image charge of opposite sign in the metallic vacuum pipe. These image charges crossing a couple of electrodes result in a response voltage signal. Then the bunch crossing through a BPM appears as a pulse as the current pass the metallic electrodes, as sketched in Figure 1.5. Furthermore, the difference between the response voltages of electrodes is proportional to the beam position in one transverse plane (Figure 1.6).

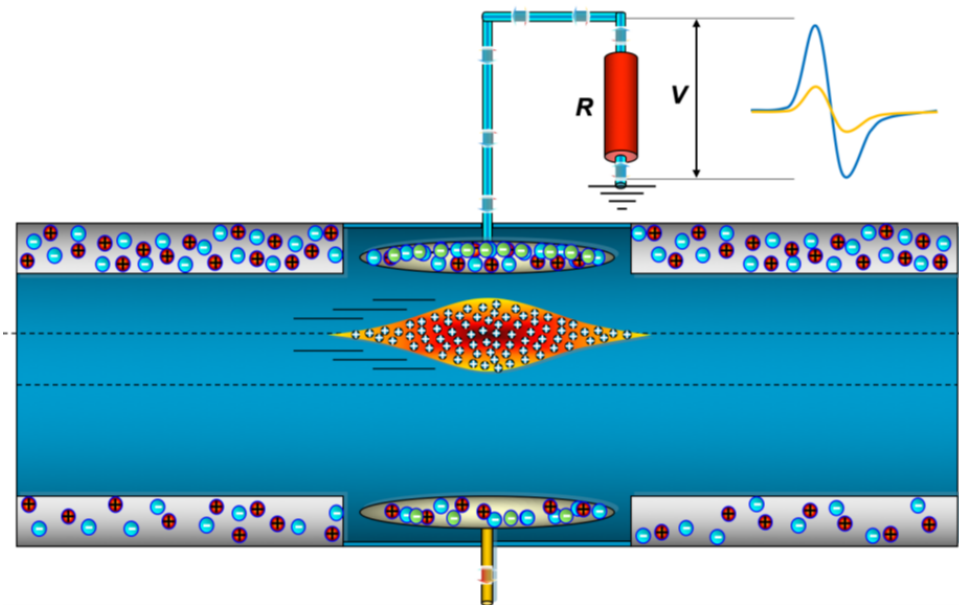


Figure 1.5: Image charges and BPM signals for a displaced beam bunch [4].

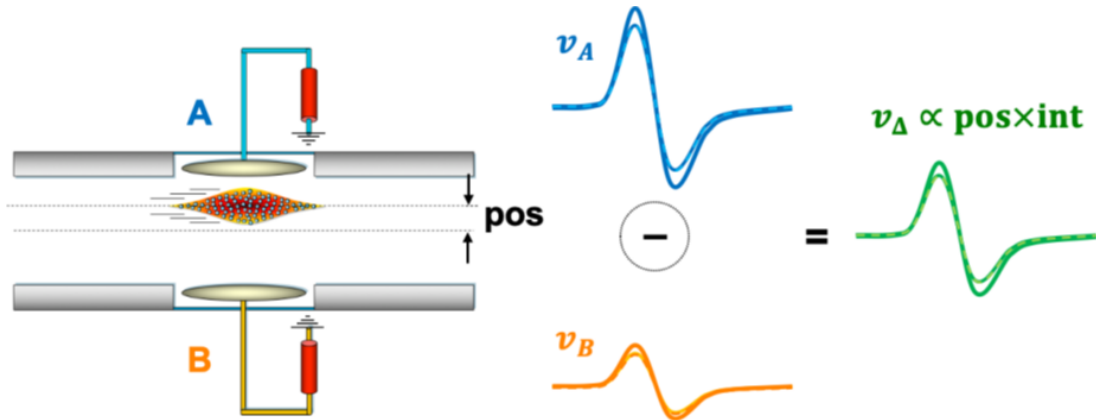


Figure 1.6: The beam (bunch) intensity effect on the difference signal of a BPM pickup [4].

### 1.1.2. Read-out electronics

Each BPM pickup is equipped with front-end electronics, processing one or both (horizontal and vertical) planes. In most cases it is preferred to locate the BPM electronics outside the accelerator tunnel to avoid damage of the semiconductors and other elements from the ionizing radiation during machine operation. This requires rather long coaxial cables, TEM transmission-lines, between the BPM pickup in the accelerator tunnel and the read-out electronics located in a gallery or service building, often installed in temperature stabilized racks. Sometimes, e.g. to detect the position of beam with very low intensity, some signal conditioning elements, e.g. pre-amplifiers, RF filters, hybrids, etc. have to be installed in the tunnel in close proximity to the BPM pickup, or a special impedance-matching network requires to be located directly on the BPM feedthrough [4].

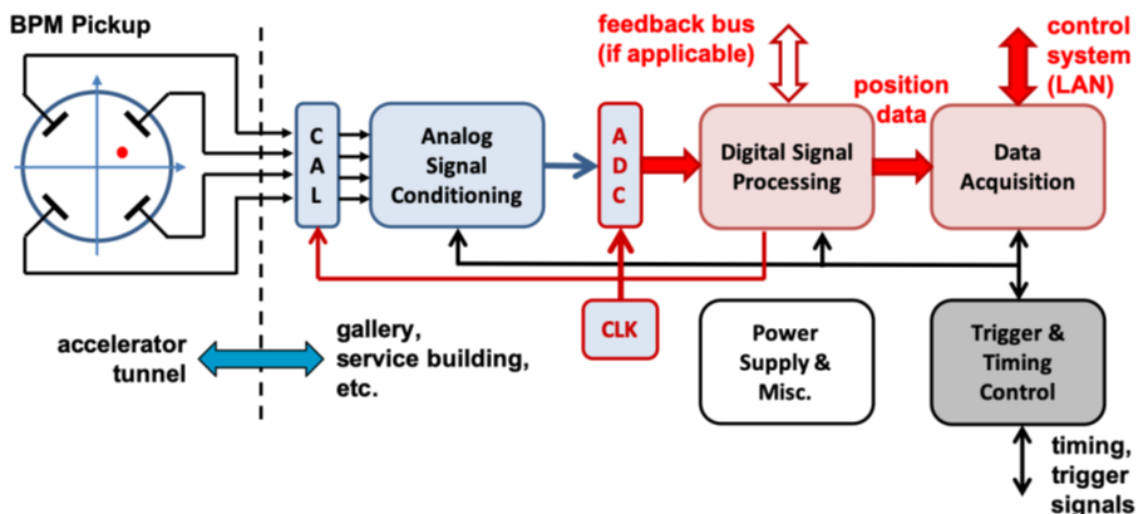


Figure 1.7: Read-out (front-end) electronics for a BPM pickup [4].

After the read-out electronics take the induced voltage from the cathodes, signals are digitalized, processed, and triggered towards the data acquisition system in order to obtain the raw data, which follow the next ASCII format. In each of those files, beam position of  $N$  turns is saved for 68 BPMs in HER, or 70 BPMs in LER, i.e. different files per ring. In the analysis present in chapters 4 and 5, this raw data format will be important, as a predecessor of a new ASCII format easier to employ in the SOMA project.

```

1 {{Metadata},
2   {("BPM_Name" -> {{x_1,x_2,x_3,x_4,x_5,.....,x_N},
3     {y_1,y_2,y_3,y_4,y_5,.....,y_N},
4     {z_1,z_2,z_3,z_4,z_5,.....,z_N}}),
5   ("BPM_Name" -> {{x_1,x_2,x_3,x_4,x_5,.....,x_N},
6     {y_1,y_2,y_3,y_4,y_5,.....,y_N},
7     {z_1,z_2,z_3,z_4,z_5,.....,z_N}}),
8   (.....,
9   .....,
10  )}}

```

Listing 1.1: Generic format of BPM raw data including name or ID and beam position coordinates per turn.

---

# 2

---

# Optics Concepts in Accelerator Physics

---

A circular collider such as SuperKEKB is composed of several magnets with multipoles of different orders. Dipoles are used to bend the particles to keep them in a circular path and to form the ring. The horizontal force  $F$ , which is orthogonal to the trajectory, is provided by the vertical magnetic field  $B_y$  of dipoles as  $F = evB_y = \gamma m_0 v^2 / \rho$ , which bends the particles with a radius,

$$\rho = \frac{p}{eB_y} \quad (2.1)$$

This equation is the well known *magnetic-rigidity* of the accelerator. On the other hand, quadrupoles are used to focus the beam to a focal point, similar to photons with lenses. The basic cell to build an accelerator is called FODO cell. Such cells present an alternating placement of focusing and defocusing quadrupoles with other type of magnets (dipoles, sextupoles, etc...) and Radiofrequency cavities in between, as shown in Figure 2.1. Those cells are usually repeated many times along the whole ring. This focusing-defocusing movement of particles means beam oscillations around the ideal particle trajectory, either in both the transverse plane and the longitudinal coordinate. In this chapter and for our interest, transverse oscillations are covered with the approach followed by the one explained in [8].

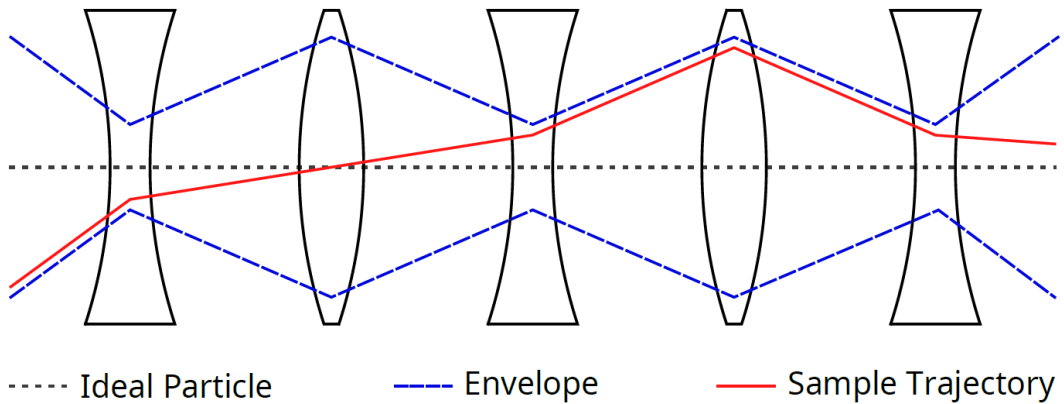


Figure 2.1: FODO cells, a basic cell composed of two drift spaces, a focusing and a defocusing quadrupole [9].

## 2.1. Equation of motion

The motion of particles in a storage ring is described by *Hill's differential equation* for motions with periodic focusing properties,

$$\frac{d^2u}{ds^2} + k(s)u = 0 \quad (2.2)$$

Where the variable  $u$  represents the transverse coordinates  $x$  and  $y$ . The function  $k(s)$  is a non-constant restoring force, and is periodic with the circumference  $C$  of the storage ring ( $k(s + C) = k(s)$ ). In a quadrupole field with gradient  $g$ , the field strength  $k(s)$  is given by,

$$k = \frac{eg}{p} \quad \text{for the horizontal plane} \quad (2.3)$$

$$k = -\frac{eg}{p} \quad \text{for the vertical plane} \quad (2.4)$$

And in a dipole field of bending radius  $\rho$  given by Equation (2.1),  $k(s)$  is given by,

$$k = \frac{1}{\rho^2} \quad \text{for the horizontal plane} \quad (2.5)$$

$$k = 0 \quad \text{for the vertical plane} \quad (2.6)$$

## 2.2. Linear Transfer Map

The final position of a particle after passing through an accelerator element can be described using transfer maps. In the case of linear optics, and in analogy with light optics, these maps take the form of matrices in the phase space. Thus, the position of a particle at the longitudinal position  $s$  can be calculated as a function of its position at  $s_0$  using the transport matrix.

$$\begin{pmatrix} u \\ u' \end{pmatrix}_s = \begin{pmatrix} m_{11} & m_{12} \\ m_{21} & m_{22} \end{pmatrix} \cdot \begin{pmatrix} u \\ u' \end{pmatrix}_{s_0} \quad (2.7)$$

Here  $u$  is the particle transverse displacement from the reference orbit and  $u' = du/ds$  is the angle between its trajectory and the reference orbit. An important assumption comprehends the motion in the horizontal and vertical planes is independent, i.e. the particle motion in  $x$  and  $y$  is uncoupled. In any ring of an accelerator, the main regions can be divided into free spaces and magnets where the magnetic field is linear and constant in the longitudinal direction  $s$  of the element.

### 2.2.1. Drift Space

In a drift space or field free region, the particle follows a straight line and the solution of Equation (2.2) for  $k = 0$  is,

$$u(s) = u_o + (s - s_o)u'_o \quad (2.8)$$

$$u'(s) = u'_o \quad (2.9)$$

Where  $u_0$  is the position and  $u'_0$  is the angle of the particle at the beginning of the field free region. A drift space section of length  $L$  is represented by the following matrix,

$$M_{drift} = \begin{pmatrix} 1 & L \\ 0 & 1 \end{pmatrix} \quad (2.10)$$

### 2.2.2. Dipole Magnets

For a dipole, the magnetic field is constant, with a  $k = 1/\rho^2$  value for the horizontal plane and zero in the vertical plane (for the vertical plane the solution is identical to the drift space case). The transport matrix for the horizontal plane is then,

$$M_{dipole} = \begin{pmatrix} \cos(L/\rho) & \rho \sin(L/\rho) \\ -1/\rho \sin(L/\rho) & \cos(L/\rho) \end{pmatrix} \quad (2.11)$$

### 2.2.3. Quadrupole Magnets

The value of  $k$  in a quadrupole magnet has the same sign as the gradient  $g = \partial B_y / \partial x = \partial B_x / \partial y$  in the horizontal plane and opposite sign in the vertical plane (see Equations (2.3)-(2.4)). For  $k > 0$ , the quadrupole magnetic field is focusing and the trajectory of the particle is given by the solution,

$$u(s) = \cos(\sqrt{k}(s - s_o)) u_o + \frac{1}{\sqrt{k}} \sin(\sqrt{k}(s - s_o)) u'_o \quad (2.12)$$

The transport matrix of a focusing field region of length  $L$  is,

$$M_{focusingquad.} = \begin{pmatrix} \cos(\sqrt{k}L) & \frac{1}{\sqrt{k}} \sin(\sqrt{k}L) \\ -\sqrt{k} \sin(\sqrt{k}L) & \cos(\sqrt{k}L) \end{pmatrix} \quad (2.13)$$

If  $k < 0$ , the quadrupole is defocusing and the trajectory of a particle is given by,

$$u(s) = \cosh(\sqrt{|k|}(s - s_o)) u_o + \frac{1}{\sqrt{|k|}} \sinh(\sqrt{|k|}(s - s_o)) u'_o \quad (2.14)$$

The transport matrix of a defocusing field region of length  $L$  is,

$$M_{defocusingquad.} = \begin{pmatrix} \cosh(\sqrt{|k|}L) & \frac{1}{\sqrt{|k|}} \sinh(\sqrt{|k|}L) \\ \sqrt{|k|} \sinh(\sqrt{|k|}L) & \cosh(\sqrt{|k|}L) \end{pmatrix} \quad (2.15)$$

Importantly, these maps should be symplectic, meaning the area of the phase-space ellipse is preserved (Figure 2.2), ensuring that the particle's motion is accurately represented [9]. In this way, the matrix  $M_{FODO} = M_{focusingquad.} \cdot M_{drift} \cdot M_{defocusingquad.} \cdot M_{drift}$  represents the transfer map of a particle through a FODO cell. For a closed machine, a full revolution can be described by a so-called one-turn map, being the transfer matrix of the whole machine, denoted  $M$ , shown in Equation (2.16). Such a map can potentially contain thousands of elements.

$$\begin{pmatrix} z \\ z' \end{pmatrix}_s = M \cdot \begin{pmatrix} z \\ z' \end{pmatrix}_{s_0} \quad (2.16)$$

## 2.3. Twiss Functions

We expect a solution of the Hill's equation in the form of a quasi-harmonic oscillation: amplitude and phase will depend on the position  $s$  in the ring. This solution which satisfies Equation (2.2) is of the form,

$$u(s) = a\sqrt{\beta(s)} \cos(\mu(s) + \psi) \quad (2.17)$$

Here  $\beta$  and  $\mu$  are periodic functions with periodicity  $C$ , while  $a$  and  $\psi$  are constants depending on initial conditions. The function  $\beta$  is called *beta-function* or *amplitude function* and  $\mu$  is called *phase function* or *betatron phase*, which is related to the beta-function by,

$$\mu(s_2) - \mu(s_1) = \int_{s_1}^{s_2} \frac{1}{\beta(s)} ds \quad (2.18)$$

As a charge travels around the ring it executes a lateral oscillation which is neither harmonic nor periodic. The motion is a kind of distorted sine-wave with a varying amplitude ( $a\sqrt{\beta(s)}$ ) which is modulated in proportion to the root of the betatron function, and with a phase  $\mu(s)$  which advances with  $s$  at a varying rate proportional to  $1/\beta$ . Thus, the smaller is the  $\beta$ -function, the smaller is also the envelope of the beam. The integral around the ring (i.e.  $s_2 = s_1 + C$ ) is  $2\pi Q$ , where  $Q$  is the *Tune* or number of betatron oscillations per revolution.

$$Q = \frac{1}{2\pi} \oint \frac{1}{\beta(s)} ds \quad (2.19)$$

The beta-function, the phase function, and the *alpha function*, which is defined as the derivative of the  $\beta$ -function, are called the *Twiss functions*.

$$\alpha(s) = -\frac{1}{2} \frac{d\beta(s)}{ds} \quad (2.20)$$

The sign of the alpha function at a certain point in the ring gives information whether the trajectories of particles are convergent (+ sign) or divergent (- sign). While the equation of motion and the transport matrices given in section 2.2 describe the movement of a single particle, the Twiss functions are more suitable to describe the dynamics of the large number of particles which form the beam. For instance, the square root of the beta function is at first order directly proportional to the beam size  $\sigma$  in a dispersion free region,

$$\sqrt{\beta\varepsilon} = \sigma \quad (2.21)$$

Here  $\epsilon$  is a constant called *emittance*. The phase advance, defined as the difference of the phase function between two points  $s_1$  and  $s_2$ , is the change of the oscillation phase of particles. Finally, a difference in the  $\beta$ -function compared to the design leads, increase possibly of unstable and larger beams, degrading its properties and making it harder to control. This relative difference in  $\beta$ -function is called the *beta-beating*, which is expressed in percents as,

$$\beta\text{-beating [\%]} = \frac{\beta_z(s) - \beta_z(s)_{model}}{\beta_z(s)_{model}} \quad (2.22)$$

The  $\beta$ -beating function plays a key role in the accelerator's optics, as it remarks zones along the ring for which the amplitude of oscillations are significant compared to the design model. That function represents one of the important results in the next chapters. Figure 2.2 provides a summary and relations of the Twiss parameters as well as its geometrical interpretation.

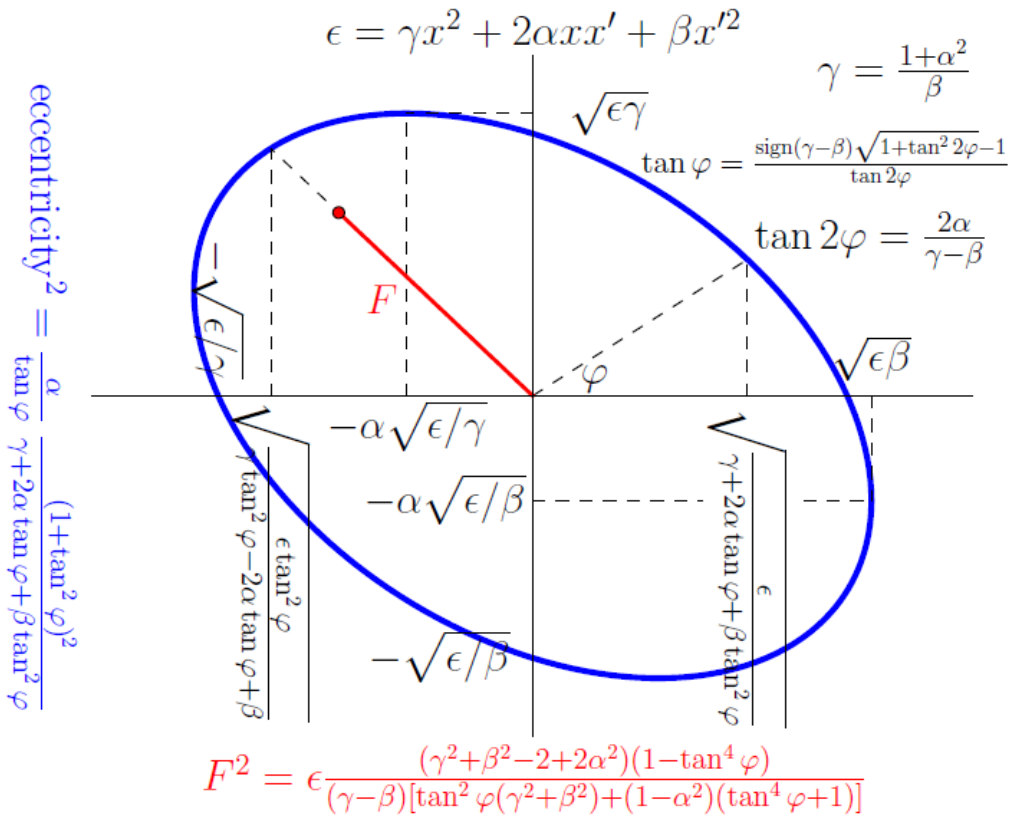


Figure 2.2: Summary of relevant quantities in the phase-space ellipse  $x'$  versus  $x$  [10].

---

**3**

---

# Resonance Driving Terms

---

Nonlinearities in the dynamics of charged particle beams can lead to resonant effects, which degrade the beam quality and stability. These effects can be characterized using the formalism of Resonance Driving Terms (RDTs). Application of this complex mathematical tool in the realm of particle accelerators is justified by two main aspects: the beam dynamics is dominated by linear potentials and nonlinearities are described with polynomial terms (multipolar expansion) whose effects are usually small perturbations making the motion quasi-periodic.

The Twiss parameters, also known as the Courant-Snyder parameters, are a good way to describe the distribution of positions and velocities of particles in the transverse plane. One caveat of using this formalism is that it is restrained to linear optics and does not address nonlinear elements, such as sextupoles or octupoles correctors. These elements generate forces that are not directly proportional to a particle's displacement from the reference trajectory [9]. In this chapter, the mathematical framework of RDTs is introduced, either with the linear lattice model as an overview of the needed mathematical tools for the description on nonlinear maps, following the description presented in [11].

## 3.1. Motivations

The simplest magnetic element in an accelerator is the dipole, which provides an homogeneous vertical field, with the drawback of two main imperfections: a strength error and a tilt of the field around the beam axis. Last one can be modeled as another orthogonal dipolar field add to the ideal dipole, as shown in the subsequent figure.

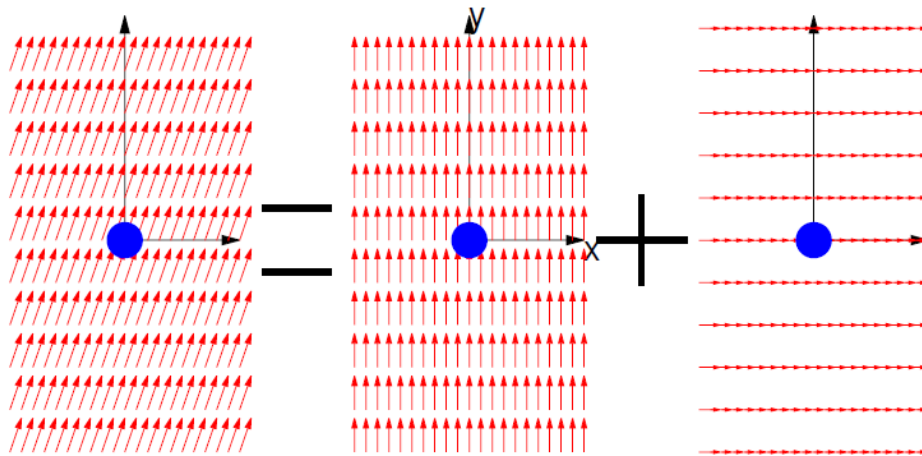


Figure 3.1: A tilted dipolar magnetic field is seen as the sum of two orthogonal magnetic fields [10].

Similarly, quadrupoles present imperfections in strength and inhomogeneities in the field: an offset field and a tilted field. The first one can be seen as the superposition of a centered quadrupole plus a dipole field, as shown in Figure 3.2, hence introducing orbit deviations. A tilted quadrupole is seen as a normal quadrupole plus another quadrupole tilted by 45°, this one is called a *skew* quadrupole, which trigger a vertical force and then an horizontal displacement. Additionally, this causes the particle motion to couple between the horizontal and vertical planes [10]. Figure 3.3 displays the decomposition of a tilted quadrupole.

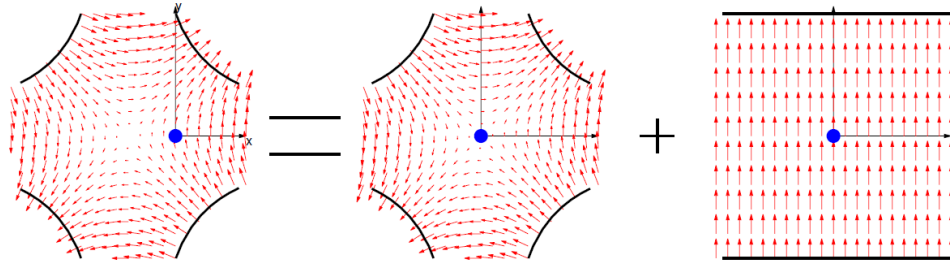


Figure 3.2: An offset quadrupole is seen as a centered quadrupole plus a dipole [10].

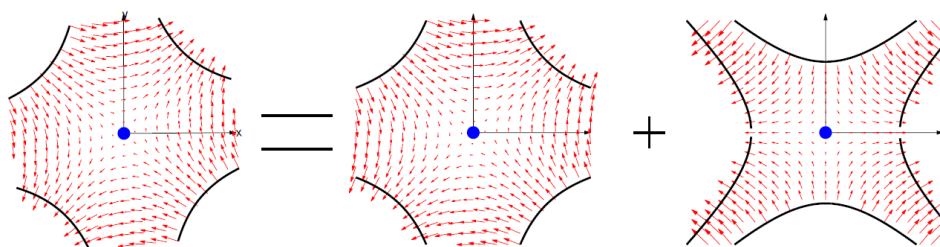


Figure 3.3: A tilted quadrupole is seen as a normal quadrupole plus another quadrupole tilted by 45° [10].

In sextupoles, an offset one is seen as a centered sextupole together with an offset quadrupole, in this way, horizontal offsets in sextupoles generate normal quadrupole perturbations while vertical offsets generate skew quadrupolar fields. An so on with high order multipole fields. Those perturbations conform the nonlinearities which this chapter intends to study and include in the optics functions of an accelerator.

## 3.2. Nonlinear Lattice

Once the beam is transversely displaced (either by fast kicker magnets or AC excitors), it experiences coherent oscillations that can be recorded Turn-by-Turn by beam position monitors (BPM). The spectrum of these oscillations can be inferred via FFT. If the lattice is free from nonlinearities the spectrum contains the betatron tune line only, whereas introducing nonlinearities secondary spectral lines appear. Before continue, some physical assumptions are set: this approach is based on a first order non-resonant normal form. Effects due to chromaticity and dispersion are not taken into account. In this chapter we refer to BPM as a pair (or two pairs if they are single-plane monitors) of pick-ups whose region in between is free of nonlinearities, namely a location where both  $x$  and  $p_x$  can be inferred exactly.

### 3.2.1. One-turn map and nonlinearities

The beam centroid at a position  $b$  is modeled as a single particle whose transport around the ring is described by one-turn symplectic map acting on the 4D vector  $\mathbf{X}_b = (x, p_x, y, p_y)|_b$ . In order to include the nonlinearities in the transport process, the Lie operator play a key role in the propagation of the Hamiltonian for each nonlinearity, as expressed in the following equation.

$$\mathbf{X}_{b,i} = M_b \mathbf{X}_{b,i-1} \quad M_b = M_{W+1} \prod_{w=1}^W e^{iH_w} M_w \quad (3.1)$$

Here  $W$  is the number of nonlinear multipoles,  $M_w$  is the linear map describing the linear elements (dipole, drift or quadrupole) between the nonlinear magnets  $w - 1$  and  $w$ . The Hamiltonian  $H_w$  and the Lie operator  $e^{iH_w}$  describe the nonlinear multipoles, and the linear map  $M_{W+1}$  is introduced to take into account the linear section between the last multipole and the position  $b$ . Figure 3.4 sketches these maps in the ring.

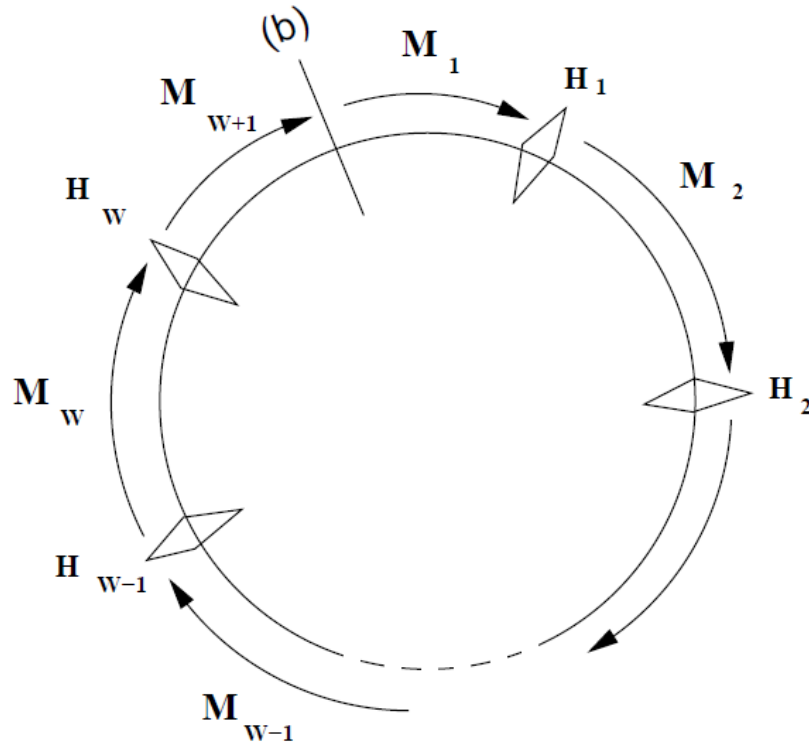


Figure 3.4: Schematic view of a ring and its transfer maps,  $M_w$  refer to sections free of nonlinearities,  $H_w$  represent the nonlinear kicks [11].

In order to simplify the description of the linear motion in the ring, a normalization map can be applied over phase-space variables employing the Twiss parameters as,

$$\begin{pmatrix} \hat{x} \\ \hat{p}_x \end{pmatrix} = \begin{pmatrix} (\beta_x)^{-1/2} & 0 \\ \alpha_x(\beta_x)^{-1/2} & (\beta_x)^{1/2} \end{pmatrix} \begin{pmatrix} x \\ p_x \end{pmatrix} \quad (3.2)$$

In transverse beam dynamics, the action is defined as the amplitude of the oscillations that the beam undergoes, it can be used as a variable to define a new transformation  $h_{q,\pm}$  with  $q$  the normalized coordinates defined in Equation (3.2), in terms of the well known *action-angle* variables  $J_q$  and  $\phi_q$ .

$$h_{q,\pm} = \hat{q} \pm i\hat{p}_q = \sqrt{2J_q} e^{\mp i(\phi_q + \phi_{q,0})} \quad (3.3)$$

For example, for the transverse coordinates  $x$  and  $y$  the transformations are,

$$h_{x,\pm} = \hat{x} \pm i\hat{p}_x = \sqrt{2J_x} e^{\mp i(\phi_x + \phi_{x,0})} \quad (3.4)$$

$$h_{y,\pm} = \hat{y} \pm i\hat{p}_y = \sqrt{2J_y} e^{\mp i(\phi_y + \phi_{y,0})} \quad (3.5)$$

In these new coordinates, the one-turn map simplifies to,

$$M_b = \prod_{w=1}^W e^{\cdot \tilde{H}_{bw} \cdot R} \quad (3.6)$$

With  $R$  the rotation matrix describing the linear motion and  $\tilde{H}_{bw}$  is the Hamiltonian expressed in the new coordinates propagated by the map describing the linear lattice between the observation point  $b$  and the  $w$ -th multipole. Then, defining the new 4D vector phase-space as,

$$\mathbf{h}_w = (h_{w,x,+}, h_{w,x,-}, h_{w,y,+}, h_{w,y,-}) \quad (3.7)$$

The propagation over one-turn is defined as,

$$\mathbf{h}_{bw} = M_b \cdot M_{b+1} \cdots M_w \mathbf{h}_w \quad (3.8)$$

In those coordinates called complex Courant-Snyder coordinates, the above relation is a rotation whose angle is the phase advance between the points  $w$  and  $b$  (as the propagation is a linear map composition the actions  $J_{x,y}$  do not change), then with  $h_{bw,q,\pm} e^{\mp i \Delta \phi_{w,q}^b}$  the new Hamiltonian becomes,

$$\tilde{H}_{bw} = H_w(\mathbf{h}_{bw}) \quad (3.9)$$

It could be proof that using properties of the Lie operator and the Campbell-Backer-Hausdorff theorem up to the first order (see appendices of [11]), the new Hamiltonian follows,

$$\prod_{w=1}^W e^{\cdot \tilde{H}_{bw} \cdot} \simeq e^{\cdot \tilde{H}_b \cdot}, \quad \tilde{H}_b = \tilde{H}_b(J_x, J_y, \phi_x, \phi_y) = \sum_{w=1}^W \tilde{H}_{bw} \quad (3.10)$$

In this way, up to the first order, the one-turn map is factorized in a complex rotation, and the Lie operator contains the sum of all the nonlinear contributions propagated through the ring. The relevant objective is to find multipolar magnetic field perturbations in the lattice of the ring, then it is required to express the Hamiltonian in terms of the multipolar expansion.

$$H_w = -\Re \left[ \sum_{n \geq 2} (K_{n-1} + iJ_{n-1}) \frac{(x+iy)^n}{n!} \right]_w = \sum_{n \geq 2} H_w^{(n)} \quad (3.11)$$

Then, in the complex Courant-Snyder coordinates the new Hamiltonian reads,

$$\begin{aligned} \tilde{H}_w^{(n)} &= \sum_{jklm}^{n=j+k+l+m} h_{w,jklm} h_{w,x,-}^j h_{w,x,+}^k h_{w,y,-}^l h_{w,y,+}^m \\ &= \sum_{jklm}^{n=j+k+l+m} h_{w,jklm} (2J_x)^{\frac{j+k}{2}} (2J_y)^{\frac{l+m}{2}} e^{i[(j-k)(\phi_x + \phi_{x,0}) + (l-m)(\phi_y + \phi_{y,0})]} \end{aligned} \quad (3.12)$$

$$h_{w,jklm} = -\frac{[K_{w,n-1} \Omega(l+m) + iJ_{w,n-1} \Omega(l+m+1)]}{j! k! l! m! 2^{j+k+l+m}} i^{l+m} (\beta_{w,x})^{\frac{j+k}{2}} (\beta_{w,y})^{\frac{l+m}{2}} \quad (3.13)$$

Here  $\Omega(i) = 1$  if  $i$  is even or  $\Omega(i) = 0$  if  $i$  is odd. This function is introduced to select either the normal  $K_n$  or the skew  $J_n$  multipoles. Finally, from Equations (3.3) and (3.9), the Hamiltonian in the new coordinates of the one-turn map at  $b$  with nonlinearities follows the next expression, where  $\Delta\phi_{w,q}^b$  is the phase advance between the locations  $b$  and  $w$ .

$$\tilde{H}_{bw} = \sum_{j,k,l,m}^{n=j+k+l+m} h_{w,jklm} e^{i[(j-k)\Delta\phi_{w,x}^b + (l-m)\Delta\phi_{w,y}^b]} h_{w,x,-}^j h_{w,x,+}^k h_{w,y,-}^l h_{w,y,+}^m \quad (3.14)$$

### 3.2.2. Definition and Derivation of RDTs

The Hamiltonian  $H_b$  defined in Equation (3.10) depends on both the actions  $J_x, J_y$  and the phases  $\phi_{b,x}, \phi_{b,y}$ . Nonresonant normal form coordinates can be introduced to obtain a Hamiltonian (i.e. a one-turn map) depending on the action variables only, e.g.  $H_b(I_x, I_y)$ . The transformation is performed by a generating function  $F$ ,

$$\begin{aligned} F &= \sum_{j,k,l,m}^{n=j+k+l+m} f_{jklm} \zeta_{x,-}^j \zeta_{x,+}^k \zeta_{y,-}^l \zeta_{y,+}^m \\ &= \sum_{j,k,l,m}^{n=j+k+l+m} f_{jklm} (2I_x)^{\frac{j+k}{2}} (2I_y)^{\frac{l+m}{2}} e^{i[(j-k)(\psi_x + \psi_{x,0}) + (l-m)(\psi_y + \psi_{y,0})]} \end{aligned} \quad (3.15)$$

Where  $\zeta_{q,\pm} = \sqrt{2I_q} e^{\mp i(\psi_q + \psi_{q,0})}$ ,  $I_q$  the new actions,  $\psi_q$  the new phases and  $\psi_{q,0}$  the new arbitrary initial conditions. The symbolic expression for the transformation is  $e^{iF} e^{i\tilde{H}} R e^{-iF} = e^{iH(I_x, I_y)} R$ . Making use again of the Campbell-Backer-Hausdorff theorem up to first order,

the generating functions terms at a certain location  $b$  are related to the hamiltonian coefficient as follows,

$$f_{jklm}^{(b)} = \frac{h_{jklm}^{(b)}}{1 - e^{2\pi i[(j-k)Q_x + (l-m)Q_y]}} = \frac{\sum_w h_{w,jklm} e^{i[(j-k)\Delta\phi_{w,x}^b + (l-m)\Delta\phi_{w,y}^b]}}{1 - e^{2\pi i[(j-k)Q_x + (l-m)Q_y]}} \quad (3.16)$$

Where the sum is over all the nonlinear elements and  $\Delta\phi_b^w$  is the phase advance between the  $w$ -th multipole and the location  $b$ . Complex variables  $f_{jklm}$  (at any location) are called *Resonance Driving Terms* (RDTs), and they diverge when a resonance occurs, i.e. when,

$$(j - k)Q_x + (l - m)Q_y = p, \quad \text{where } p \in \mathbb{N} \quad (3.17)$$

Those resonances are related to the optics of the accelerator. Figure 3.5 left shows a tune diagram where the fractional part of tunes  $Q_x$  and  $Q_y$  can be related to resonance lines excited by multipoles up to decapoles ( $n = 5$ ). It becomes apparent that the diagram fills quickly when considering further orders, as shown Figure 3.5 right. Thankfully, the higher the multipole order, the weaker the resonances usually are as their introduced perturbations are usually smaller. This makes choosing a working point possible, even if some particles are hitting resonance lines [9].

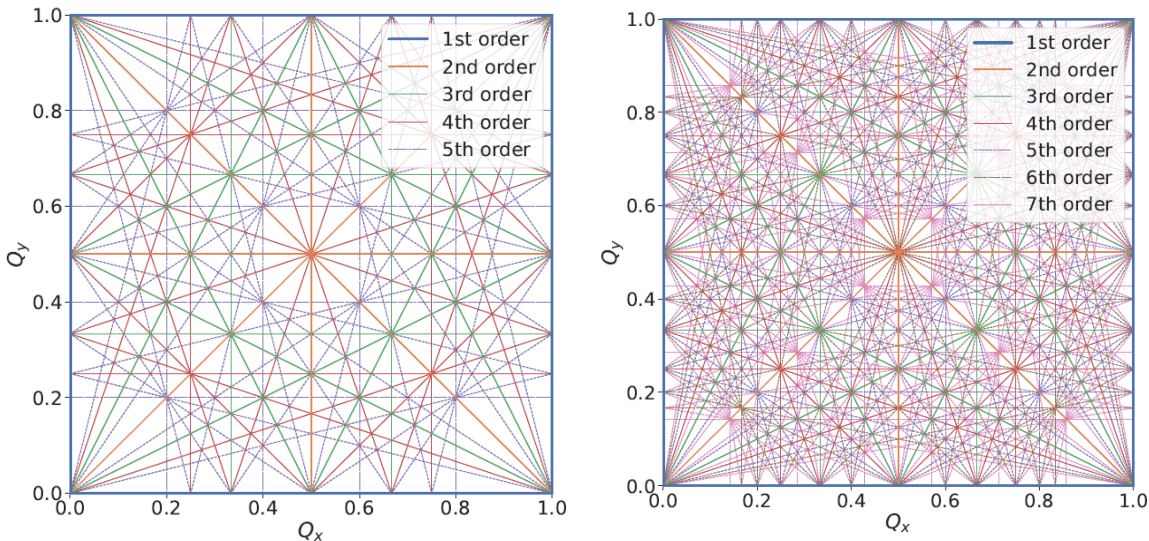


Figure 3.5: Tune diagram with resonance lines excited by different multipole orders.  
Resonances lines up to decapoles ( $n \leq 5$ ) for left and up to decatetrapole ( $n \leq 7$ ) for right [9].

As a transformation of first order, it is possible to calculate the inverse transformation truncated also to the first order to obtain,

$$h(N) = e^{iF(N)} \zeta(N) \simeq h(N) + [F(N), \zeta(N)] \quad (3.18)$$

$$\begin{aligned} h_{x,-}(b, N) &= \sqrt{2I_x} e^{i(2\pi\nu_x N + \psi_{b,x,0})} \\ &- 2i \sum_{jklm} j f_{jklm}^{(b)} (2I_x)^{\frac{j+k-1}{2}} (2I_y)^{\frac{l+m}{2}} e^{i[(1-j+k)(2\pi\nu_x N + \psi_{b,x,0}) + (m-l)(2\pi\nu_y N + \psi_{b,y,0})]} \end{aligned} \quad (3.19)$$

$$\begin{aligned} h_{y,-}(b, N) &= \sqrt{2I_y} e^{i(2\pi\nu_y N + \psi_{b,y,0})} \\ &- 2i \sum_{jklm} l f_{jklm}^{(b)} (2I_x)^{\frac{j+k}{2}} (2I_y)^{\frac{l+m-1}{2}} e^{i[(k-j)(2\pi\nu_x N + \psi_{b,x,0}) + (1-l+m)(2\pi\nu_y N + \psi_{b,y,0})]} \end{aligned} \quad (3.20)$$

The nonlinear tunes  $\nu_{x,y}$  appear in the above expression instead of  $Q_{x,y}$  introduced in (3.16), since this approach takes into account possible detuning due to either linear coupling or amplitude dependent effects. Expressions (3.19) and (3.20) have the following form,

$$\begin{aligned} h_{q,-}(b, N) &= a_{q,0}^{(b)} e^{i2\pi N \nu_q} + \sum_{jklm} a_{jklm}^{(b)} e^{i2\pi N (\theta_{j,k} \nu_x + \omega_{l,m} \nu_y)} \\ a_{q,0}^{(b)}, a_{jklm}^{(b)} &\in \mathbf{C}, \quad \theta_{j,k}, \omega_{l,m} \in \mathbf{N} \end{aligned} \quad (3.21)$$

The first term is the *fundamental* or *tune line*. Its position in the spectrum provides the fractional part of the tune  $\nu$ . The secondary lines contained in the summation are instead generated by the nonlinear magnets and depend on the RDTs  $f_{jklm}$ .

### 3.2.3. Frequency Spectrum

From last equations, it is clear that resonance driving terms have an impact on the transverse motion of a particle. Each RDT  $f_{jklm}$  can be observed in either one or both planes, at multiples of  $Q_x \pm Q_y$ . The respective amplitude and phases of the RDTs in the horizontal  $H$  and vertical  $V$  spectrums, coming from the summation of nonlinear terms in Equations 3.19-3.20 are given by respectively,

$$H(1-j+k, m-l) = 2 \cdot j |f_{jklm}^{(b)}| (2I_x)^{\frac{j+k-1}{2}} (2I_y)^{\frac{l+m}{2}} \quad (3.22)$$

$$\phi_{(1-j+k, l-m)} = \phi_{b,jklm}^f + (1-j+k)\psi_{b,x,0} + (m-l)\psi_{b,y,0} - \frac{\pi}{2} \quad (3.23)$$

$$V(k-j, 1+m-l) = 2 \cdot l |f_{jklm}^{(b)}| (2I_x)^{\frac{j+k}{2}} (2I_y)^{\frac{l+m-1}{2}} \quad (3.24)$$

$$\phi_{(k-j, 1+m-l)} = \phi_{b,jklm}^f + (k-j)\psi_{b,x,0} + (1-l+m)\psi_{b,y,0} - \frac{\pi}{2} \quad (3.25)$$

These lines are restricted to appear under certain combinations of the horizontal and vertical tunes,

$$H_{jklm} \text{ at } (1-j+k)Q_x + (m-l)Q_y ; \quad j \neq 0 \quad (3.26)$$

$$V_{jklm} \text{ at } (k-j)Q_x + (1-l+m)Q_y ; \quad l \neq 0 \quad (3.27)$$

In the case of the horizontal and vertical tune lines are represented by  $H(1,0)$  and  $V(0,1)$  respectively, their amplitudes and phases correspond to,

$$H(1,0) = \sqrt{2I_x} \quad \phi_{H(1,0)} = \psi_{b,x,0} \quad (3.28)$$

$$V(0,1) = \sqrt{2I_y} \quad \phi_{V(0,1)} = \psi_{b,y,0} \quad (3.29)$$

By reworking the previous equations, it can be seen that RDTs are factors of the line amplitude and the actions  $I_x$  and  $I_y$ ,

$$|f_{jklm}^{(b)}| = \frac{|H_{jklm}|}{2j(2I_x)^{\frac{j+k-1}{2}} (2I_y)^{\frac{l+m}{2}}} \quad (3.30)$$

$$|f_{jklm}^{(b)}| = \frac{|V_{jklm}|}{2l(2I_x)^{\frac{j+k}{2}} (2I_y)^{\frac{l+m-1}{2}}} \quad (3.31)$$

### 3.2.4. Resonance classification and nomenclature

Not all the coefficients  $f_{jklm}$  are of interest to us, since only some of them are related to the multipoles. The generic potential  $x^s y^q$  of a multipole expansion in the magnetic field selects the index  $j+k = s$  and  $m+l = q$ , as shown in table 3.1. Setting these combinations, the

number of valid RDTs grows rapidly with the magnet order  $n$ , as shown in table 3.2.

Multipole Kind	$n$	Potential Term	Index Relations
Norm. Quad. $x$	2	$x^2$	$j + k = 2 \quad m + l = 0$
Norm. Quad. $y$	2	$y^2$	$j + k = 0 \quad m + l = 2$
Skew Quad.	2	$xy$	$j + k = 1 \quad m + l = 1$
Norm. Sext. 1	3	$x^3$	$j + k = 3 \quad m + l = 0$
Norm. Sext. 2	3	$xy^2$	$j + k = 1 \quad m + l = 2$
Skew Sext. 1	3	$y^3$	$j + k = 0 \quad m + l = 3$
Skew Sext. 2	3	$x^2y$	$j + k = 2 \quad m + l = 1$

Table 3.1: Selection of index relative to skew quadrupole, normal and skew sextupole.

Multipole	Order	Number of poles	Number of RDTs
Quadrupole	2	4	5
Sextupole	3	6	16
Octupole	4	8	27
Decapole	5	10	50
Dodecapole	6	12	73
Decatetrapole	7	14	112
Decahexapole	8	16	151
Hectopole	50	100	23349
Kilopole	500	1000	$2.1 \times 10^7$

Table 3.2: Multipole classification by order, number of poles, and number of resonance driving terms (RDTs).

The indices sequentially select the driven resonances and their corresponding spectral lines. These spectral lines are directly associated with the RDTs listed in table 3.3 for the quadrupole case (see appendix B for spectral lines until octupole order), where the line amplitudes are obtained from Equations (3.22) to (3.25). Since the line  $H(0,0)$  is driven by two RDTs ( $f_{2100}$  and  $f_{1011}$ ), it is not considered a physical observable.

$n$	$jklm$	Type	Resonance	H-line	V-line	Amplitude H	Amplitude V
2	0020	normal	(0, 2)		(0, -1)		$4(2I_y)^{1/2}$
2	2000	normal	(2, 0)	(-1, 0)		$4(2I_x)^{1/2}$	
2	0110	skew	(-1, 1)		(1, 0)		$2(2I_x)^{1/2}$
2	1001	skew	(1, -1)	(0, 1)		$2(2I_y)^{1/2}$	
2	1010	skew	(1, 1)	(0, -1)	(-1, 0)	$2(2I_y)^{1/2}$	$2(2I_x)^{1/2}$

Table 3.3: List of spectral lines driven by resonances and corresponding RDTs, for the quadrupole case.

---

# 4

---

# SOMA Package

---

---

The SOMA package<sup>1</sup>, abbreviation of SuperKEKB Optics Measurement Analysis, is a project designed for preprocessing and analysis of Turn-by-Turn Beam Position Monitor (BPM) signals for the SuperKEKB collider. It is based on the Optics Measurements and Corrections (OMC3) python-tool and the Strategic Accelerator Design (SAD) program. OMC3 is a library for beam optics measurements and corrections used at the LHC, it contains various methods for frequency analysis of circular particle accelerators Turn-by-Turn data, as well as beam optics properties computation and correction algorithms [12]. On the other hand, SAD has been developed by KEK institute and is powerful and useful in designs, simulations, commissioning, and improvement for SuperKEKB accelerator [13].

This chapter describes the sequential structure and functionality of the SOMA package, including its preprocessing pipeline, synchronization, harmonic analysis, and its outputs for post-analysis with nonlinear beam dynamics.

## 4.1. Raw data and Preprocessing

The database is composed of several days of data taken over the working year 2024, each one containing different measurements of one ring (see Figure 1.2), and then a respective file at different times. On certain days, special measurements were made, with horizontal or vertical kicks to the beam, at injection, or with different kickers. The raw data are taken directly from the DAQ system of SuperKEKB, without any preprocessing (as explained in 1.1.2). In this way, each file contains up to 4096 turn measurements, for each coordinate

---

<sup>1</sup>Up to date project at <https://github.com/JacquelineKeintzel/SOMA.git>

$x$ ,  $y$  and  $z$ , and per each BPM in the ring. Then, each file name is stored with the format "RING\_YYYY\_MM\_DD\_hh\_mm\_ss.data". For example, for one sample of raw data taken at June 17 - 2024 with a horizontal kick, "HER\_2024\_06\_17\_17\_53\_37.data" is the corresponding file. Figures (4.1) and (4.2) show the beam centroid position in both transverse planes, for different BPMs contained in that file.

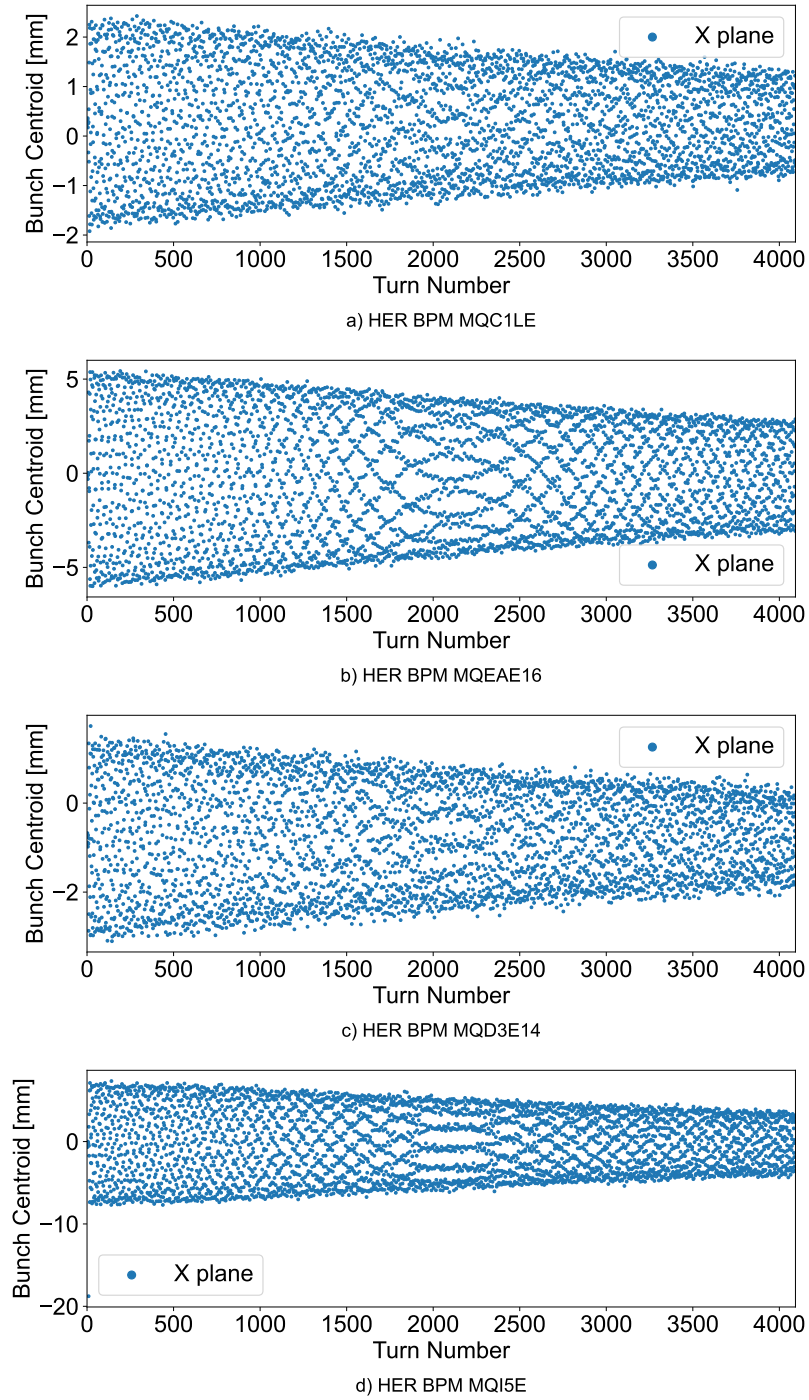


Figure 4.1: Beam position for the horizontal component, from some BPMs in the HER ring. Measurements taken on June 17 - 2024 at 17h 53m.

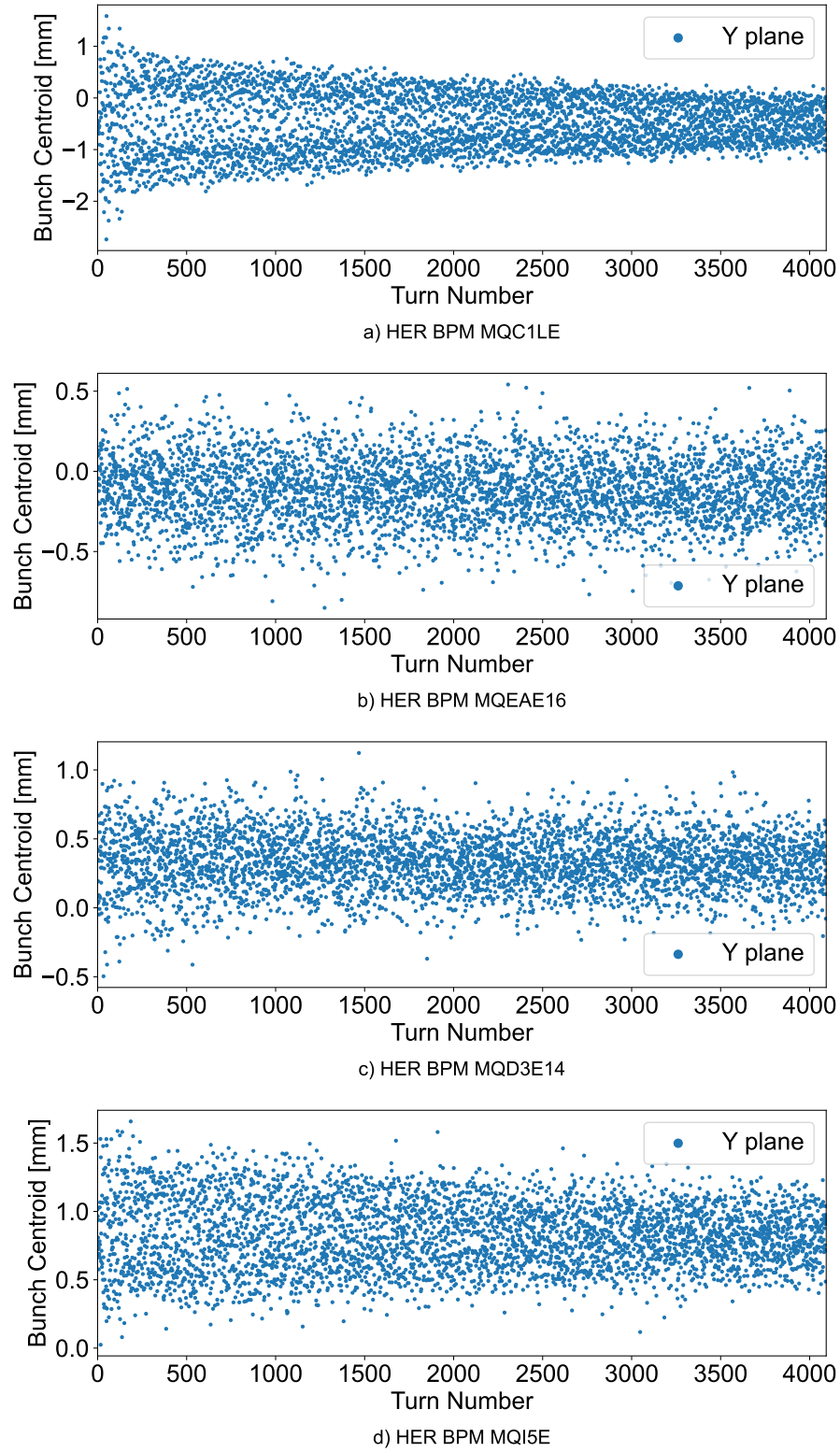


Figure 4.2: Beam position for the vertical component, from some BPMs in the HER ring.  
Measurements taken on June 17 - 2024 at 17h 53m.

In order to run the harmonic analysis, it is required to convert the raw data into a sdds format,

to be compatible with OMC3 process. The sdds format basically includes some metadata values from the BPM system, and includes just the Turn-by-Turn values of transversal planes  $x-y$ , which are the ones of interest for the upcoming analysis. The next listing shows the sdds format, in which, for each BPM is assigned a value of 0 for the raw corresponding to the horizontal plane and 1 for the vertical plane. This process is now included in SOMA as a first step for the whole analysis. At the same time, SOMA calculates the tune values for both  $x-y$  planes, and includes this in the metadata of each sdds file, the fractional or decimal part of tunes will become important in section 4.3.1. From here and ahead, we assume that BPM data is in sdds format. Additionally, SOMA requires a lattice file containing all the optics parameters used on the measurement day, for the whole ring of SuperKEKB. Those parameters include magnets strengths, apertures, monitors, among others. In this way, SOMA has a model for propagation and calculation of twiss parameters and optics quantities.

```

1 # SDDSASCIIFORMAT v1
2 # Beam: SuperKEKB          RingID
3 # Acquisition date: 06/30/2025 16:38:06
4 # number of turns :        4096.0000000
5 # number of monitors :     68.0000000
6 # Opticsfile : optics$file
7 # tunes of optics$file : Qx = 45.5390000, Qy = 43.5750000
8 # File Info:
9 # - Created by : a SAD KEK to ASCII SDDS converter
10 # - Written by : A. Wegscheider, R. Yang;
11 # edit A. Koval (19) and J. Keintzel(24)
12 # - Version    : 1.0 (15.02.2024)
13 o MQC1LE   x_1      x_2      x_3      x_4      ....      x_N
14 1 MQC1LE   y_1      y_2      y_3      y_4      ....      y_N
15 o MQC2LE   x_1      x_2      x_3      x_4      ....      x_N
16 1 MQC2LE   y_1      y_2      y_3      y_4      ....      y_N
17 . ....
18 . ....

```

Listing 4.1: Generic format of BPM sdds ASCII data.

## 4.2. Harmonic Analysis

### 4.2.1. First Harmonic Analysis

The BPM Turn-by-Turn data is fundamental to measure optics parameters around the accelerator. Betatron oscillations represent highly correlated signals among BPMs. This feature can be used to reduce the BPM noise by discarding the signals with low correlation levels. Singular Value Decomposition (SVD) is used for this purpose [10]. The OMC3 project includes a tool for SVD denoising, which is applied for SOMA to the data. This is enough for a first harmonic analysis, in which Harpy<sup>2</sup> module from OMC3 denoised and calculate the FFT of BPM measurements, giving as output the amplitudes and the frequencies in the Fourier space, as it is displayed in Figure 4.3 for one random BPM in the high energy ring.

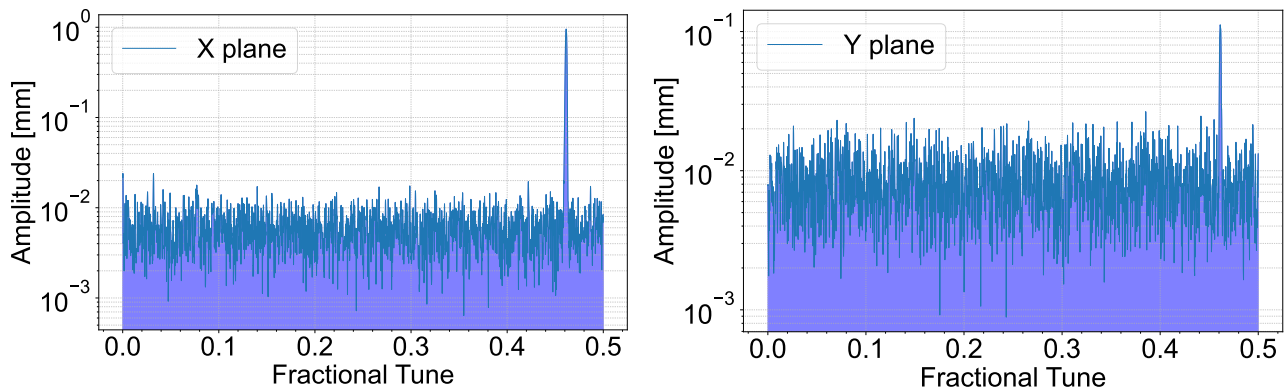


Figure 4.3: Spectra in the Fourier Space of the fractional tune from BPM MQD3E1, for both transverse planes. Measurement taken from June 17 - 2024.

From the last plots, the main peaks correspond to the fractional part of the horizontal tune  $Q_x$  (see Equation (3.21)), calculated previously in the sdds conversion, and related directly with the betatron function (see Equation (2.19)). Vertical tune is obscure by noise background as the excited plane (the horizontal one) presents large displacements in contrast with the vertical plane.

### 4.2.2. Synchronization

It is important to note that due to the non-synchronization between BPMs (no master clock), BPM data is not synchronized with respect to each other for each file. By this, it is required to a synchronization step before the harmonic analysis. Figures 4.4 and 4.5 show a colormap of the phase advance between BPMs for each measurement.

<sup>2</sup>New harmonic analysis algorithm <https://pylhc.github.io/omc3/modules/harpy.html>

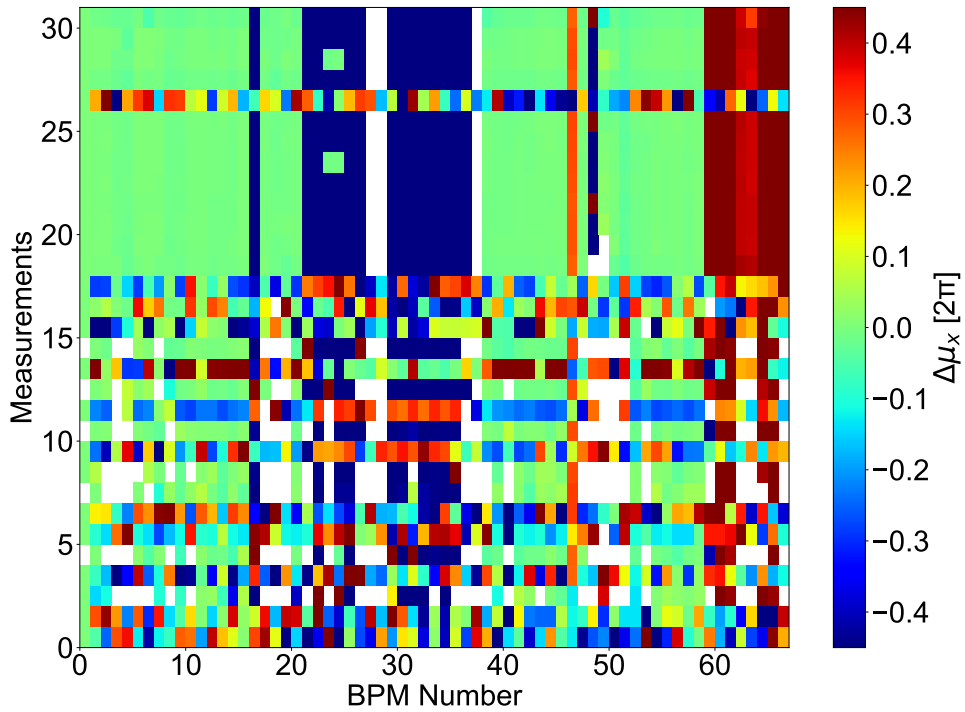


Figure 4.4: Map of the horizontal phase advance  $\Delta\mu_x$  between all the BPMs in the HER ring, for all the measurements of June 17 - 2024. An important note this is before synchronization.

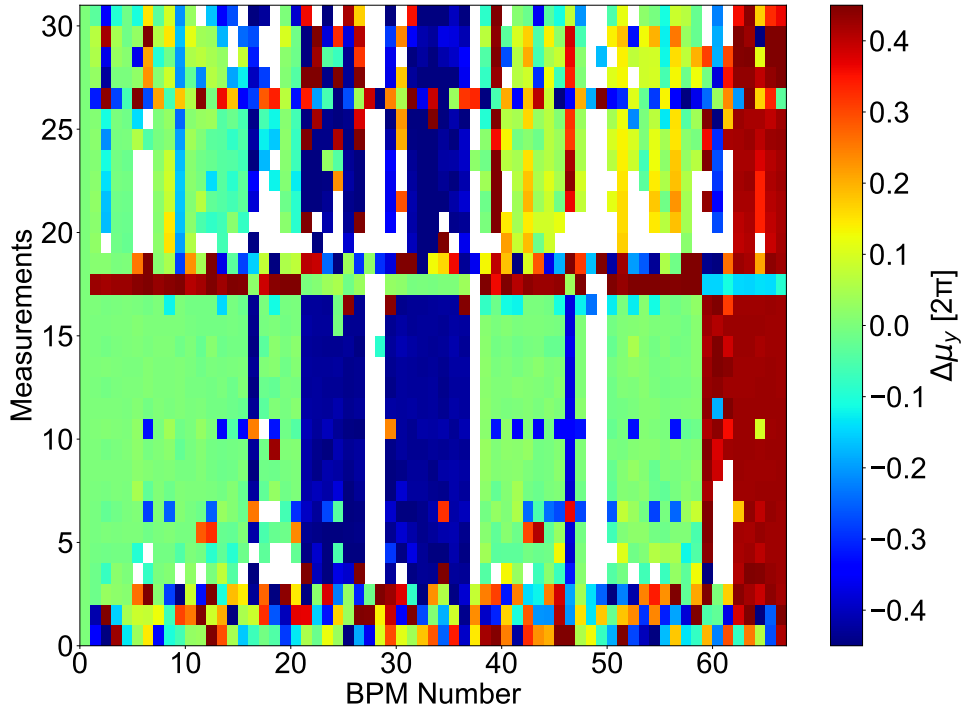


Figure 4.5: Map of the vertical phase advance  $\Delta\mu_y$  between all the BPMs in the HER ring, for all the measurements of June 17 - 2024. An important note this is before synchronization.

From those plots, it is clear measurements are asynchronous between each other, in this way SOMA provides a method to synchronized files, adjusting the universal time for which each BPM detects the beam passing through itself, and then providing a structure of Time Series to all measurements. Figures 4.6 and 4.7 sketch the respective colormaps of our example from June 17, after the synchronization step.

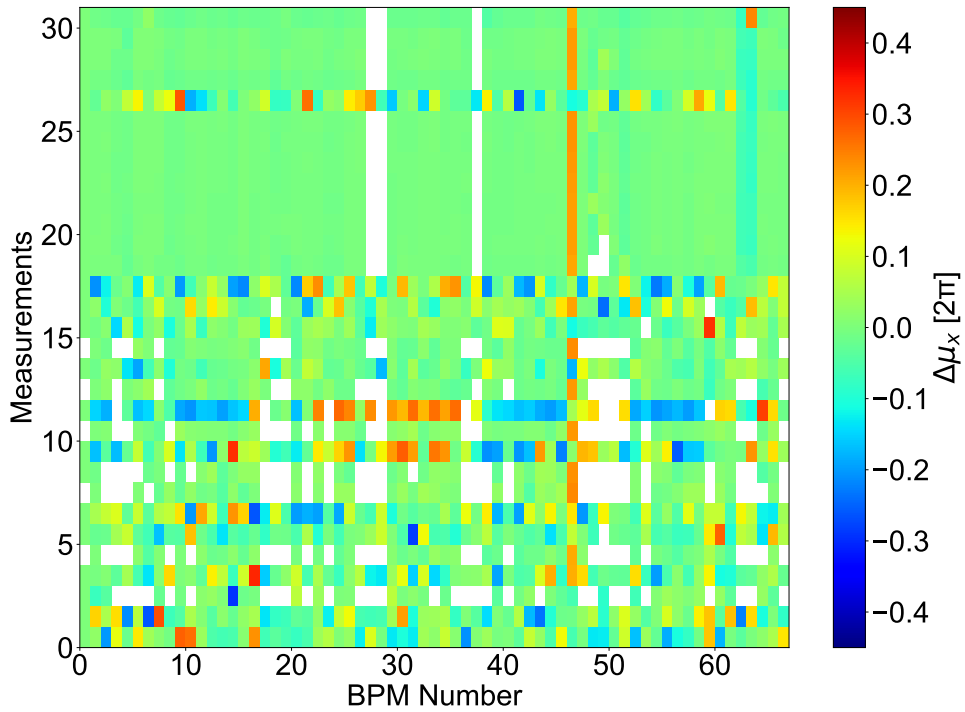


Figure 4.6: Map of the horizontal phase advance  $\Delta\mu_x$  between all the BPMs in the HER ring, for all the measurements of June 17 - 2024. This case is after synchronization.

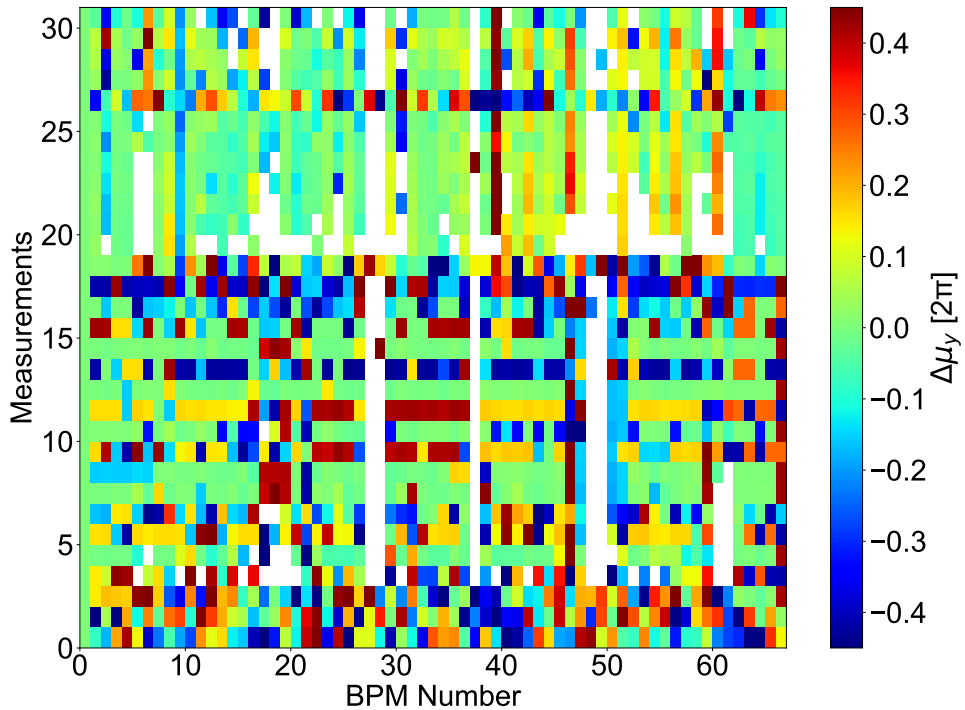


Figure 4.7: Map of the vertical phase advance  $\Delta\mu_y$  between all the BPMs in the HER ring, for all the measurements of June 17 - 2024. This case is after synchronization.

From the horizontal map, it is clear the effects of synchronization process, where files 19 to 26 are highly correlated with a difference phase advance closed to zero. However, the vertical case is quite more difficult to syncronized, due to a high sensitivity and noise in the vertical plane, but it is possible to observe a better synchronization in the same range of files.

### 4.2.3. Second Harmonic Analysis

After synchronization of the sdds data, the harmonic analysis is run again to calculate the fractional tune through the same algorithm Harpy. Figures 4.8 and 4.9 present the synchronized spectra of some BPMs in  $x$  and  $y$  planes.

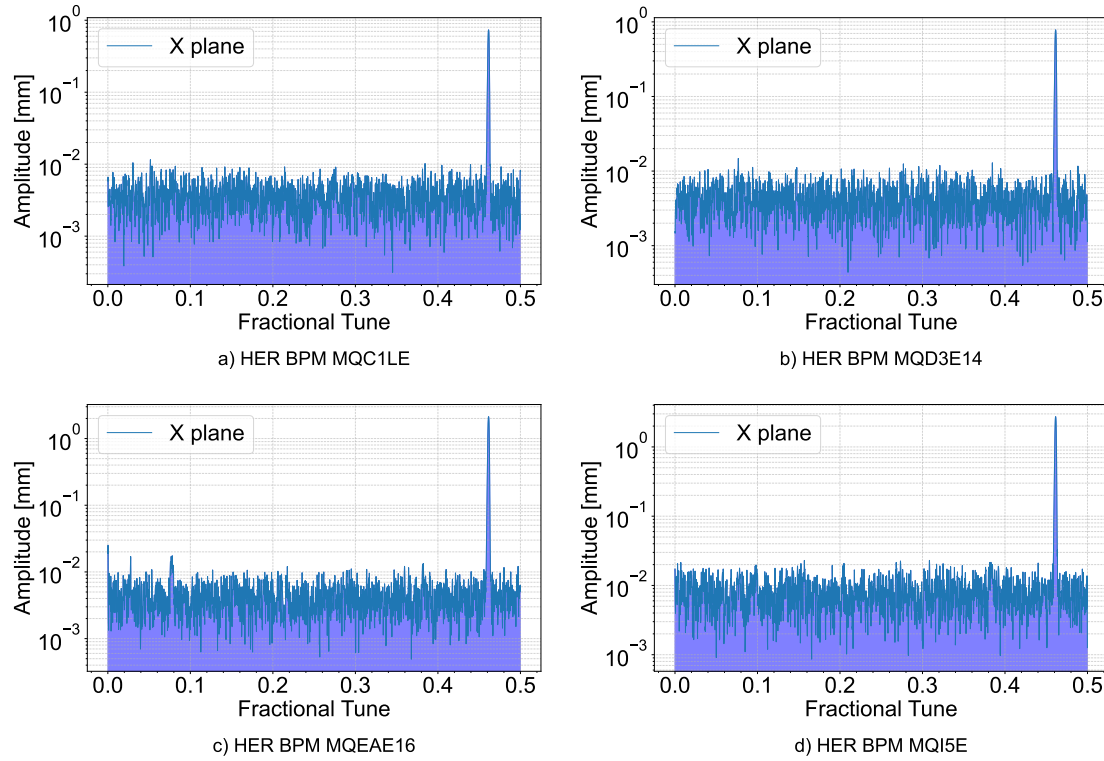


Figure 4.8: Fractional tune of some BPMs in the HER ring from measurements taken in June 17 - 2024. Amplitudes corresponding to the horizontal component.

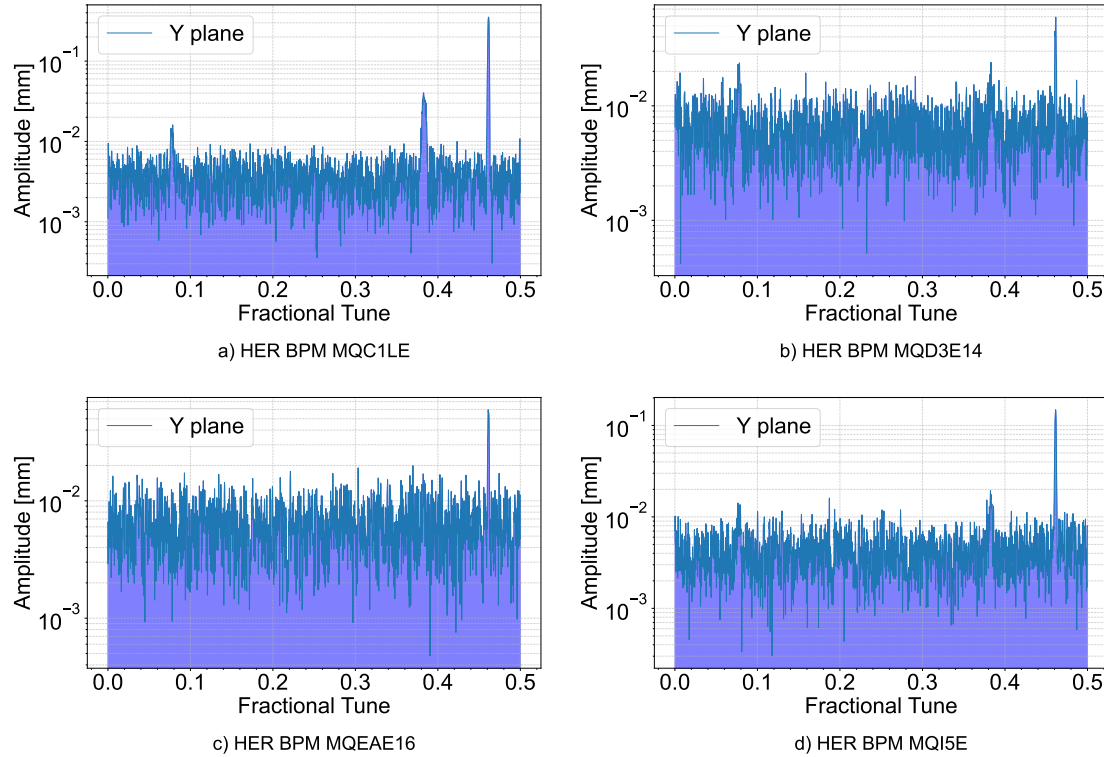


Figure 4.9: Fractional tune of some BPMs in the HER ring from measurements taken in June 17 - 2024. Amplitudes corresponding to the vertical component.

Clearly, in the horizontal plane of those examples, there are not many peaks as those with more prominence in the vertical plane. The main resonance in  $x$ - $y$  planes corresponds to the tune  $Q_x = 1 - 0.539 = 0.461$  (0.539 refers to the fractional part of tune calculated in metadata of section 4.1), and appears in both as the movement in these planes is coupled. Majority of nonlinearities in the horizontal plane are obscured by noise level, which is consistent with the horizontal kick in those measurements. On the other hand, due to high sensitivity of BPMs in the vertical plane, imperfections or high order perturbations from some resonances are significantly measured on this sample of that measurement day.

## 4.3. Optics Analysis

The observation of coherent betatron oscillations provides accurate measurements of the optics functions in the ring. The phase of betatron oscillations can be measured at the beam position monitors with the Turn-by-Turn data acquisition [8], in order to obtain the beta-beating function, phase advance and Resonance Driving Terms (RDTs). SOMA package includes a method to obtain the optics analysis automatically. Figures 4.10 and 4.11 sketch an example of beta-beating function, as well as Figures 4.12 and 4.13 sketch the phase advance along the ring, both obtained for our example of June 17 - 2024.

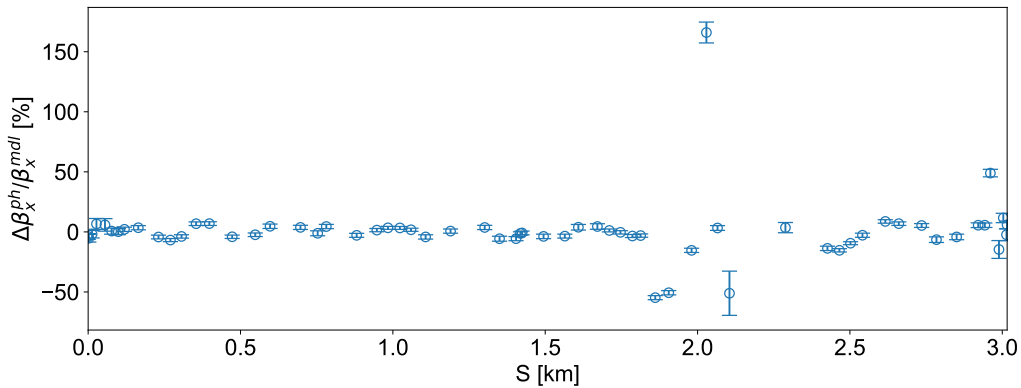


Figure 4.10: Horizontal Beta-beating function vs BPM longitudinal position in the HER obtained by SOMA code.

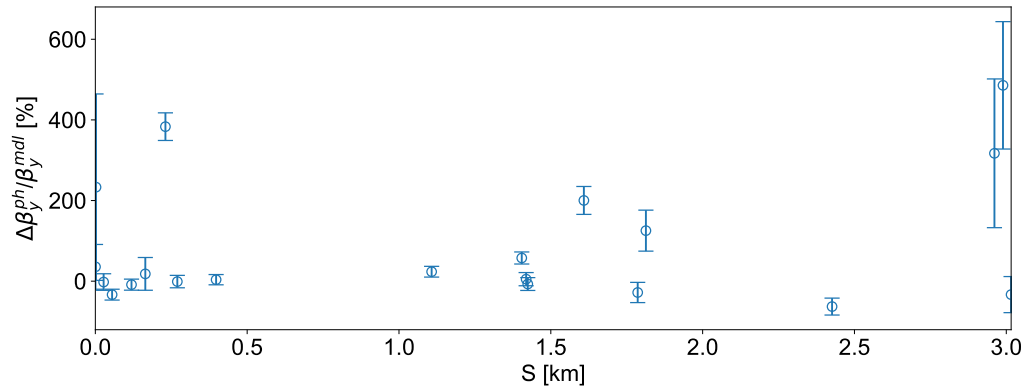


Figure 4.11: Vertical Beta-beating function vs BPM longitudinal position in the HER obtained by SOMA code.

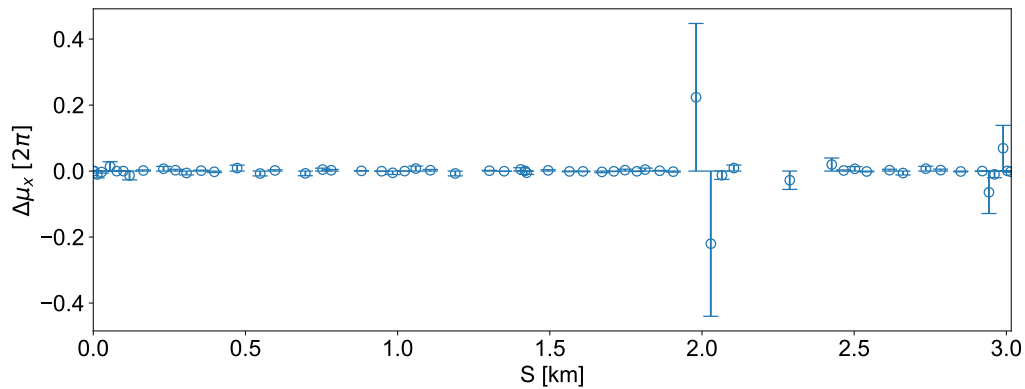


Figure 4.12: Horizontal Phase advance function vs BPM longitudinal position in the HER obtained by SOMA code.

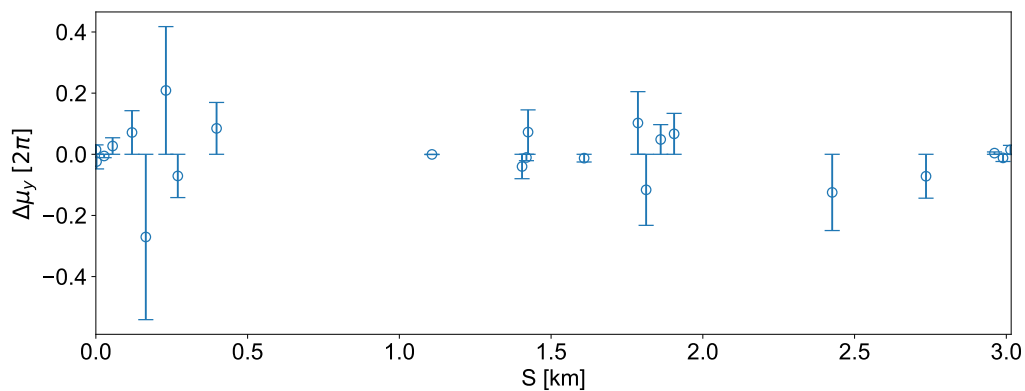


Figure 4.13: Vertical Phase advance function vs BPM longitudinal position in the HER obtained by SOMA code.

The previous Figures have something in common, they shows a constant tendency with some off measurements with large error bars. That is a consequence of the well tuned system of op-

ties from the collider team, but at the same time, reflects the deficient signal detection from some BPMs. Those monitors are called Faulty BPMs, and its malfunctioning depends on several factors, such as changes in temperature, vibrations, electronics, radiation or outdated components.

#### 4.3.1. RDTs

Following the definition of the RDTs (expressed in Equation (3.16)),  $f_{jklm}$  has a combination of four indexes. As explained in subsection 3.2.4, not all the combinations of indexes are interested for measuring nonlinear contributions on the optics (see table 3.1). In fact, corrections can reach certain level in the multipolar expansion, due by limitations in the magnets characterization. In this way, appendix B presents a summary of relevant RDTs until octupolar expansion, which can be measured by the Turn-by-Turn analysis. As seen in Equations (3.16) and (3.13), RDTs are complex numbers proportional to the strength of the field. Therefore, the complex amplitude can provide the strength contribution of a given multipolar field in the whole ring. SOMA has a method to obtain some relevant RDTs until octupolar expansion, doing an average of the contributions of nonlinearities over several measurements. For convenience, the average is over the 8 synchronized measurements found in subsection 4.2.2. Figures 4.14-4.15 present some examples of RDTs for skew octupolar fields, while Figures 4.16-4.17 present some examples of RDTs for normal octupolar fields, cases of interest to study.

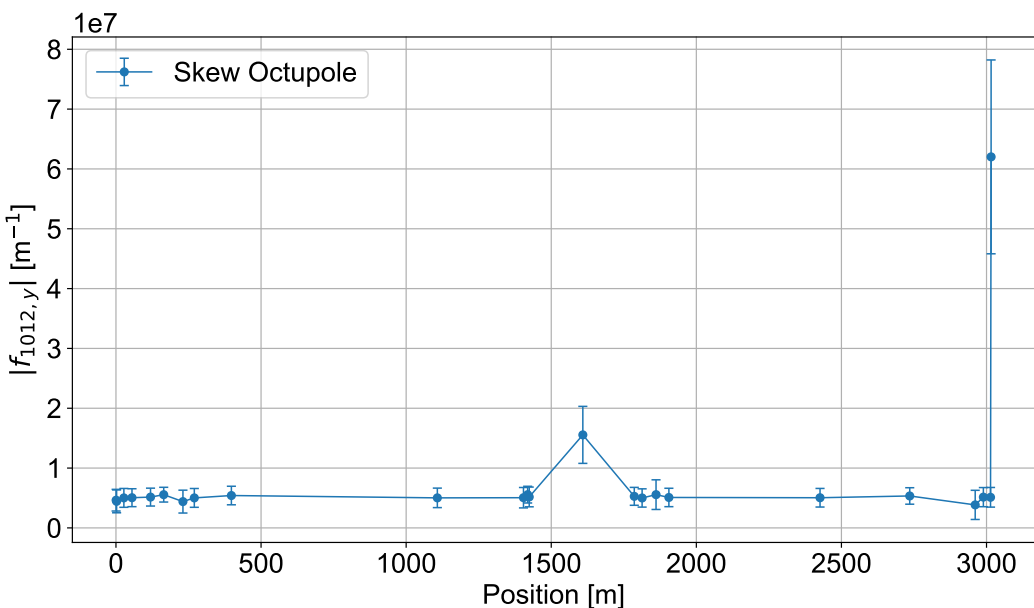


Figure 4.14: Skew Octupolar RDT  $f_{1012}$  measured in HER for the vertical plane.

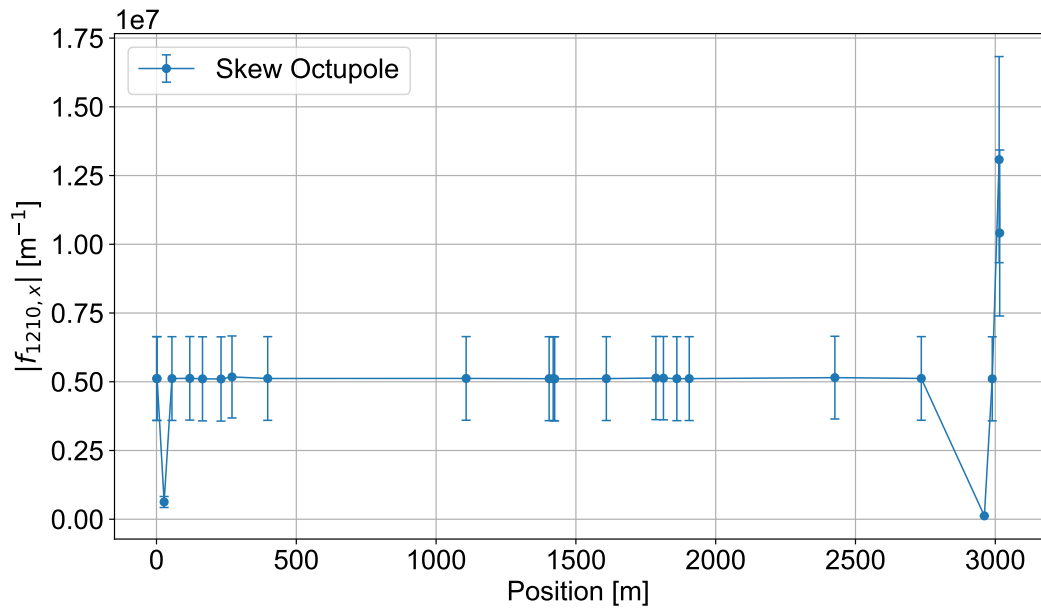


Figure 4.15: Skew Octupolar RDT  $f_{1210}$  measured in HER for the horizontal plane.

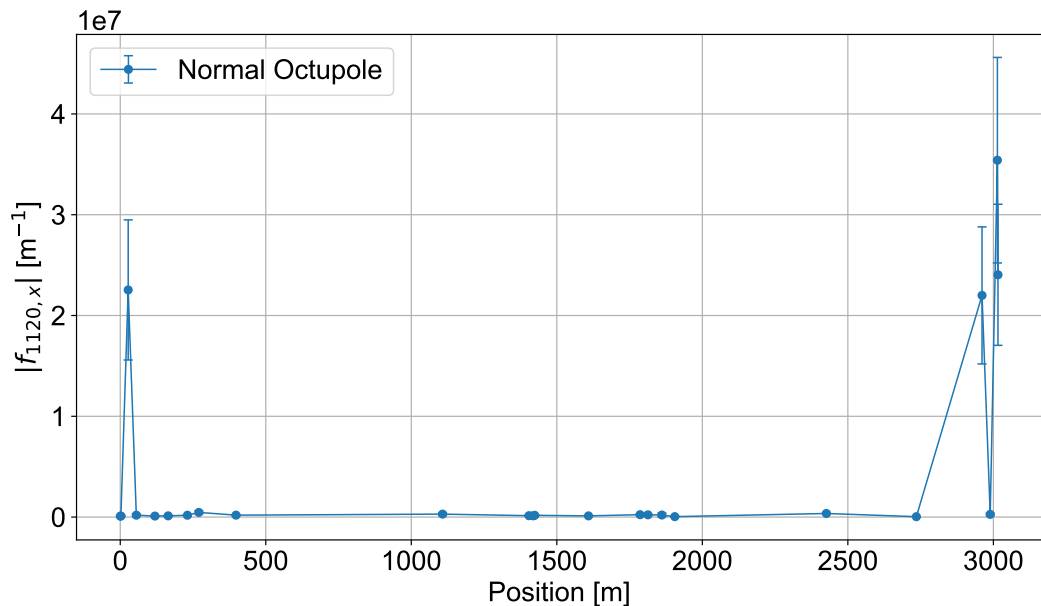


Figure 4.16: Normal Octupolar RDT  $f_{1120}$  measured in HER for the horizontal plane.

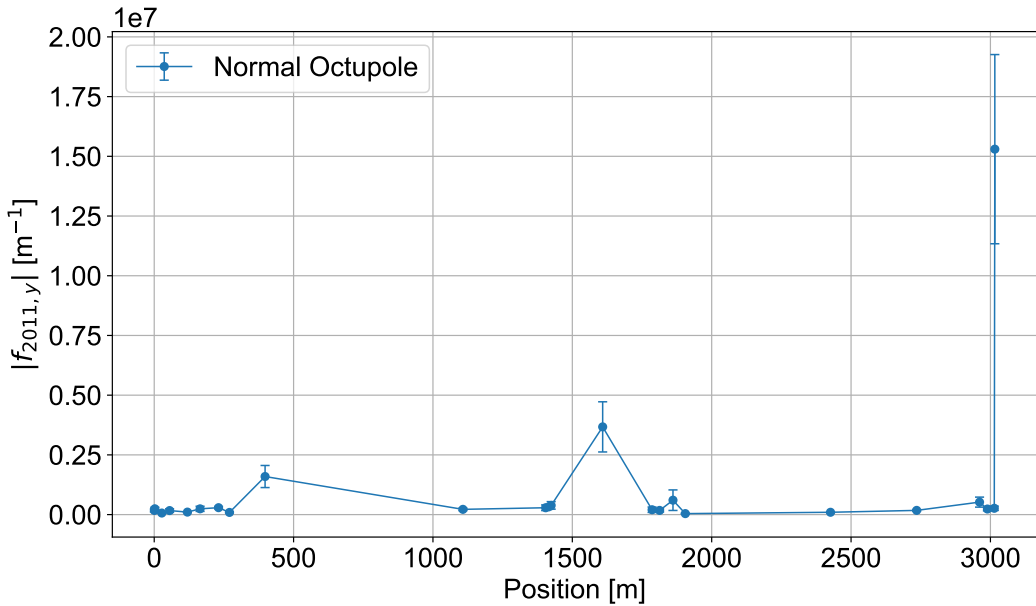


Figure 4.17: Normal Octupolar RDT  $f_{2011}$  measured in HER for the vertical plane.

In order to understand the connection between the resonances driving terms and those peaks in the second harmonic analysis, it is important to remark that the amplitude of one peak in the spectrum results from the contribution of different resonances at the same time. For example, if it is desired to study the perturbations of skew octupolar fields along the vertical plane of the ring, from amplitudes in table B.3, the choice of  $f_{1012}$  skew octupole is the most convenient. This RDT has a resonance of  $(j - k, l - m) = (1, -1)$  following Equation (3.17), then the associated horizontal and vertical amplitudes are  $H(1 - j + k, m - l) = H(0, 1)$  and  $V(k - j, 1 - l + m) = V(-1, 2)$  respectively. Nevertheless, the amplitude  $H(0, 1)$  appears also in the RDT  $f_{2101}$  and even at the quadrupole order with  $f_{1001}$ . Thus, if a resonance appears in the spectrum at  $H(0, 1) = Q_y = 0.425$  (see Equation (3.26)), it contains contributions from quadrupole and octupole orders, with quadrupole amplitude large compared to the octupole amplitude. In this way,  $f_{1012}$  is not convenient for the horizontal plane as the quadrupole order obscure the octupole contribution. Unfortunately, horizontal spectras 4.8 at 0.425 do not show a peak, as this is under the noise level of those BPMs.

On the contrary, the vertical amplitude  $V(-1, 2)$  appears at the octupole and dodecapole orders, meaning a main contribution for octupole fields. For this case, the resonance located at  $V(-1, 2) = -Q_x + 2Q_y = 0.389$  appears clearly in some spectras at Figure 4.9. BPM MQC1LE located at the region between the end and start of the ring shows a high perturbation of octupolar order, where Figure 4.14 confirms the significant contribution of  $f_{1012}$  in this regions of the HER ring. Similar analysis were realized for the octupole order from the horizontal plane, and for normal octupole fields in both planes, where results agreed the RDTs ampli-

tudes in Figures 4.15 to 4.17. Table 4.1 summarize for our case study, the resonances and where the peaks theoretically should appear in the spectras of both planes (most of them obscure by the electronics noise).

Type	RDT	Resonance	H-line	Value	V-line	Value
Skew	$f_{1012}$	$1Q_x - 1Q_y$	$1Q_y$	0.425	$-1Q_x + 2Q_y$	0.389
Skew	$f_{1210}$	$-1Q_x + 1Q_y$	$2Q_x - 1Q_y$	0.497	$1Q_x$	0.461
Normal	$f_{1120}$	$2Q_y$	$1Q_x - 2Q_y$	0.389	$-1Q_y$	0.425
Normal	$f_{2011}$	$2Q_x$	$-1Q_x$	0.461	$-2Q_x + Q_y$	0.497

Table 4.1: Skew and normal octupolar RDTs of interest, their associated resonances and the frequency spectrum lines they contribute to.

---

# 5

---

# Tracking Analysis

---

---

The previous chapter sketches the analysis with the raw data directly obtained from the rings in the accelerator. A common practice in large scale facilities regarding the performance and optimization of the machine, stay in the comparison between the experimental data with simulations covering all the physical parameters that defines each of the rings in the collider. In our case, simulations regarding the beam dynamics and optics of the bunch traveling in the pipe. In this chapter, it is displayed the simulation or tracking results, as well as its accuracy with respect to measured data.

## 5.1. Tracking data

The software required to do the simulations is provided by Mael Le Garrec [9], which make use of SAD framework to propagate the beam position centroid along the ring employing the same lattice file used for the experimental data in [4.1](#) with SOMA (i.e. the parameters of the optics for a specific date). Nevertheless, results depend on the amplitude oscillation of the kick given to the bunch, along with the transversal direction of this one. In order to set the parameters to characterize the kick, the action variable  $J$  (explained in chapter [3](#)) gives the strength in the kick to increase or decrease the amplitude. Additionally, code permits to set the direction of the kick employing the action as parameter, and the run process can include several values of action (from 0 to 30). The final result creates  $x$  and  $y$  positions in new files with the same sdds format as the employed with SOMA, each one with different amplitude oscillation. In our case, data is simulated with actions between 4.0 and 5.2. The next Figures plot some examples of tracking output.

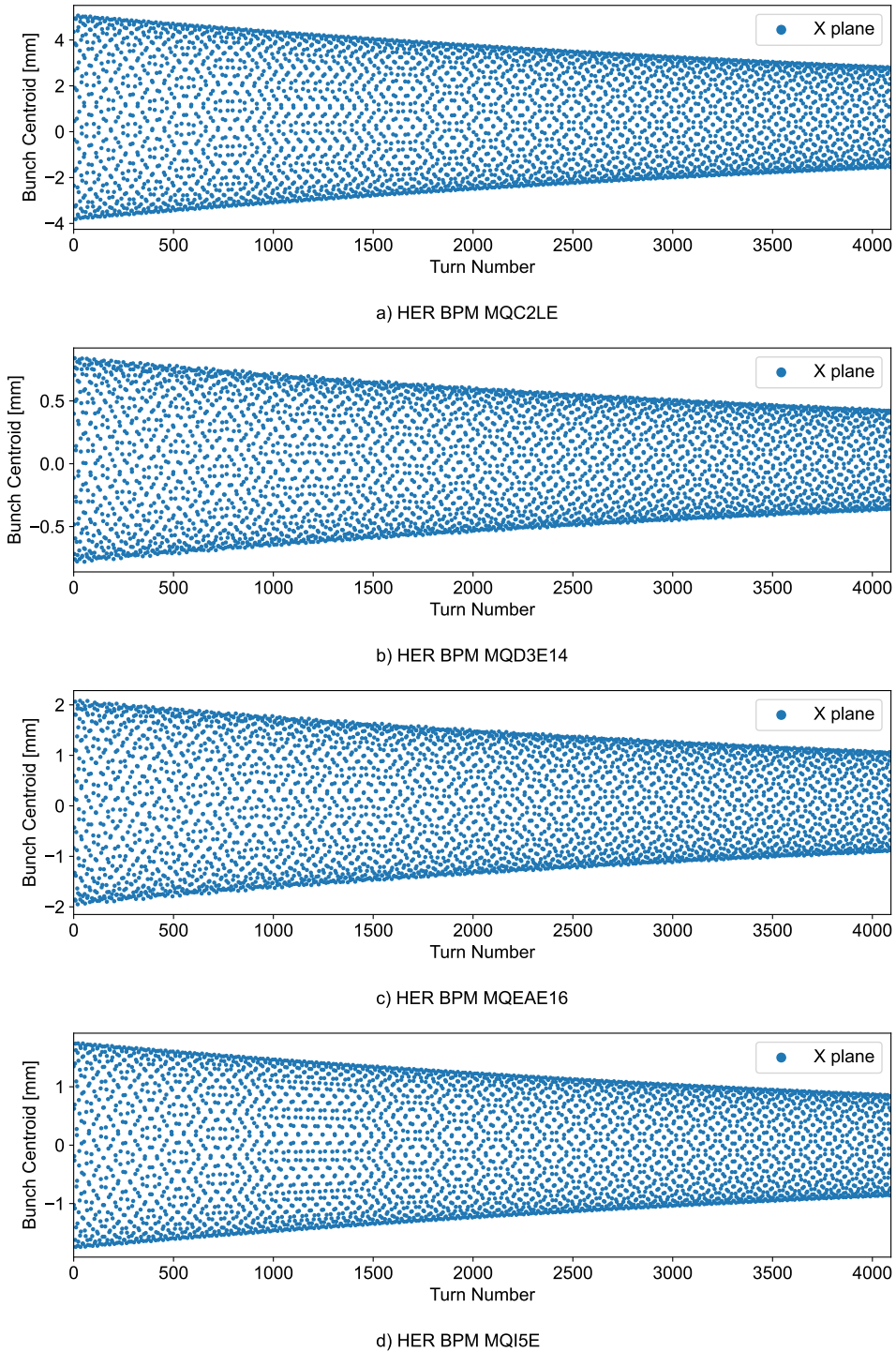


**Figure 5.1:** Tracking beam position in the horizontal component, for some BPMs in the HER ring. Lattice used is from June 17 - 2024 at 17h 53m, and with action of 4.

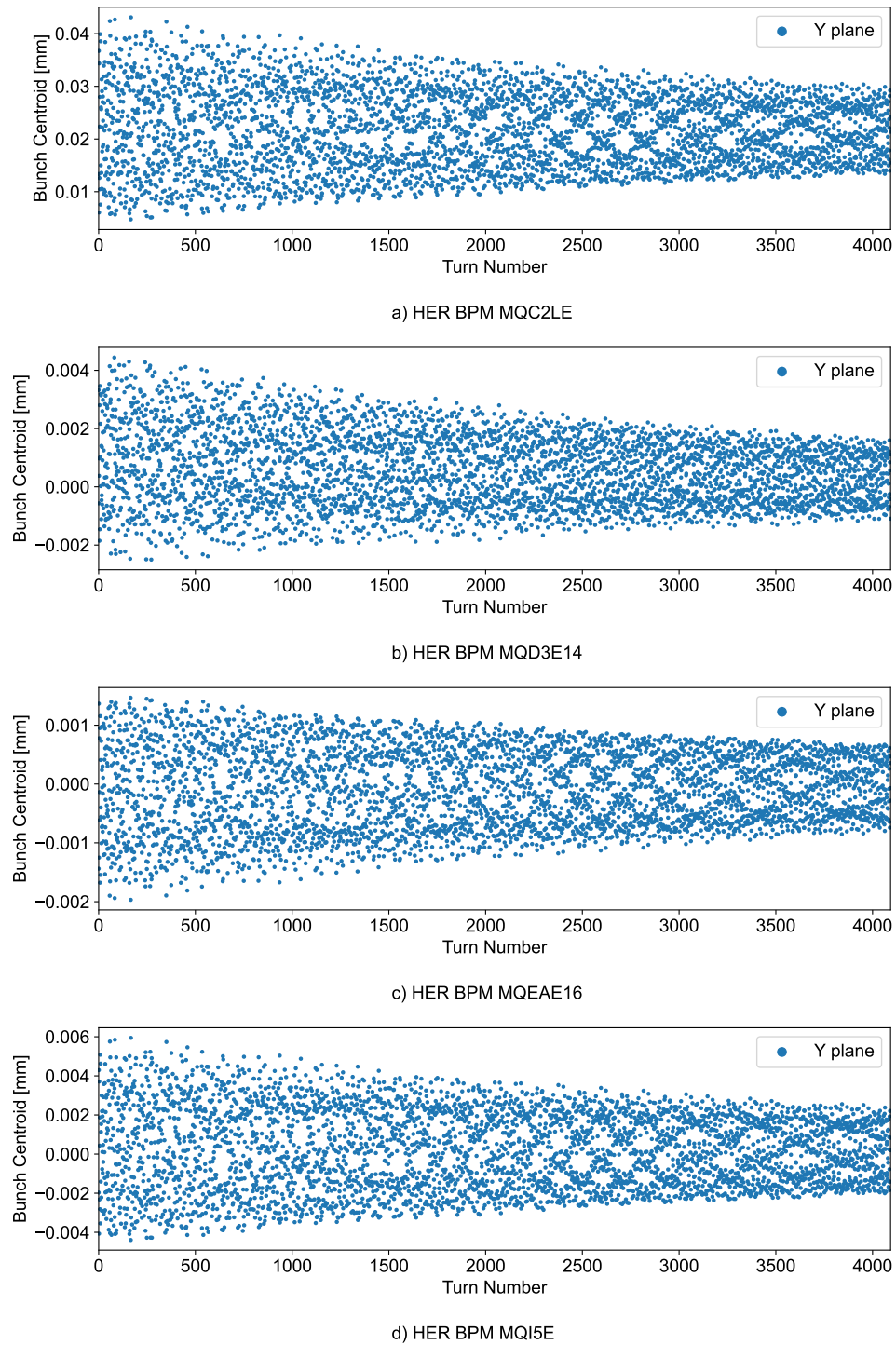


Figure 5.2: Tracking beam position in the vertical component, for some BPMs in the HER ring. Lattice used is from June 17 - 2024 at 17h 53m, and with action of 4.

## 5.2. Harmonic Analysis

Given the sdds files, the harmonic analysis follows the same as the one described in the previous chapter employing SOMA, with the difference that here is not required synchronization, as the software simulates all the BPMs data taking following a common master clock. Then Figures 5.3 and 5.4 sketch the fourier transformation of BPM tracking, for which is considered the noise deactivated and the radiation loss by the kick activated. In consequence, it is clear the amplitude order is low, reaching  $10^{-12}$  in some figures, while the main resonance or tune is at the order of  $10^{-3}$ . However, the frequency of the main peaks coincides accurate with those ones obtained in section 4.2.3. An important remark for those simulations regards the propagation of just one particle, that plays the role of the bunch centroid, the tracking code is able to simulate more than one particle and even quantum fluctuations, however, this requires high computational power, and the results do not changed significantly.

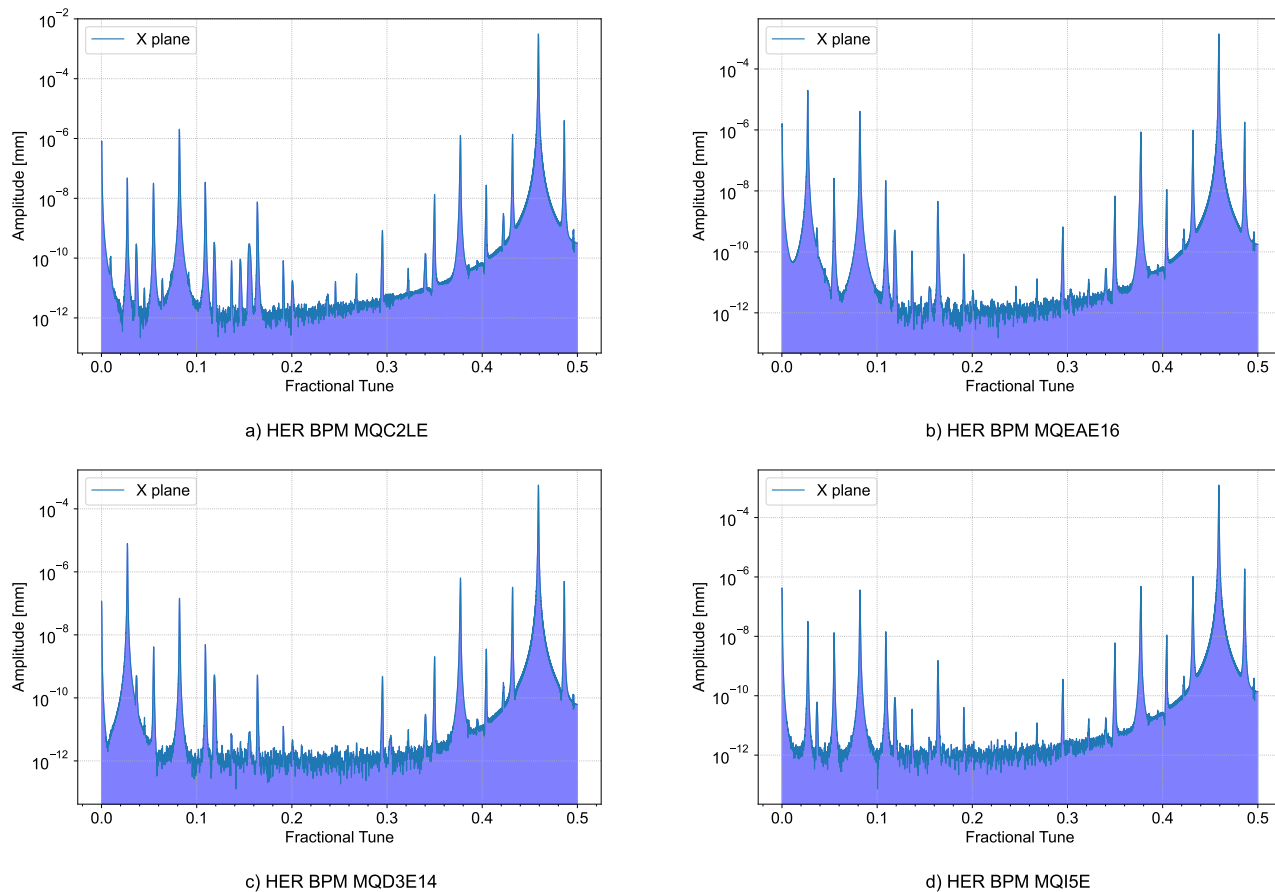


Figure 5.3: Fractional tune of some BPMs in the HER ring from simulation employing the lattice of June 17 - 2024. Amplitudes corresponding to the horizontal component and an action of 4.

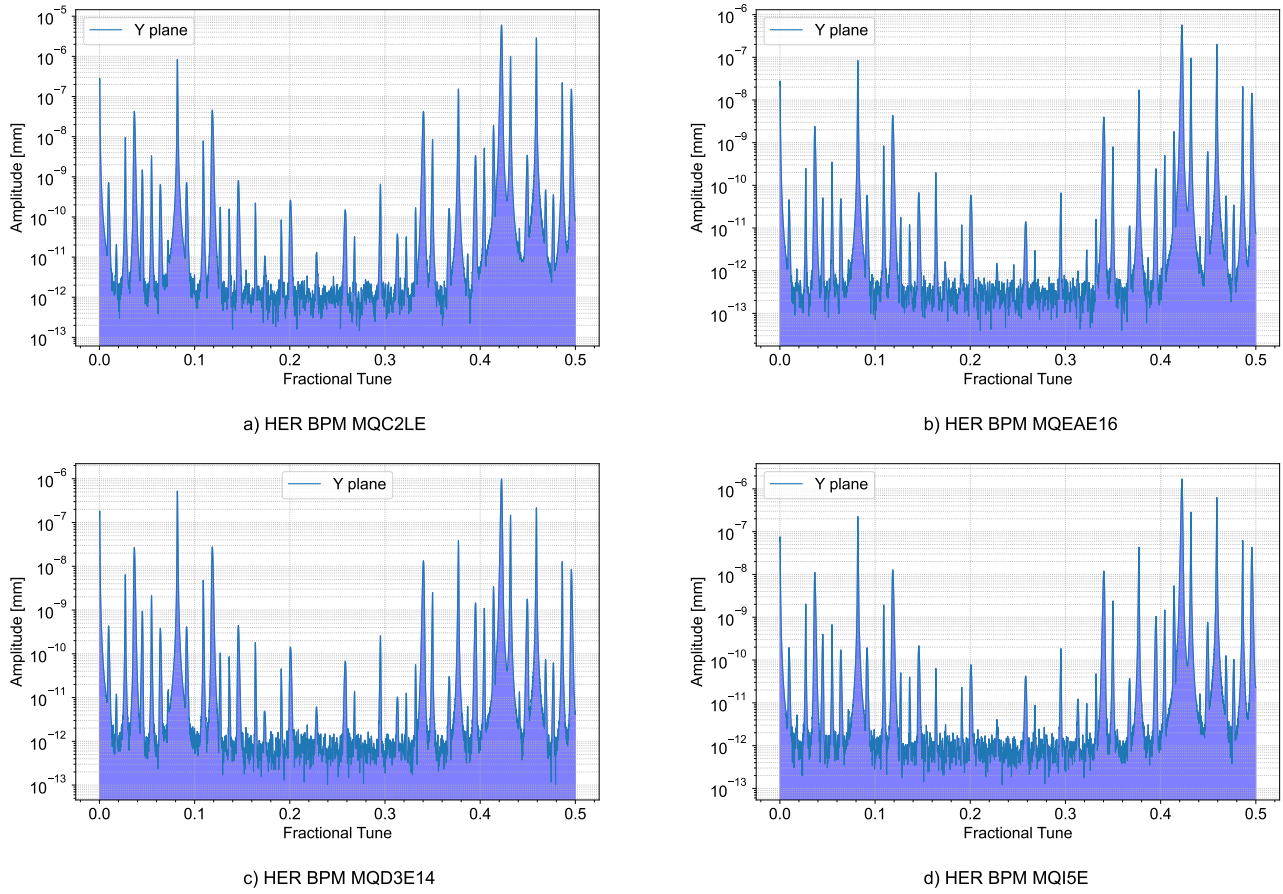


Figure 5.4: Fractional tune of some BPMs in the HER ring from simulation employing the lattice of June 17 - 2024. Amplitudes corresponding to the vertical component and an action of 4.

## 5.3. Optics Analysis

In a similar way as the chapter 4, the optics analysis is carry-on using SOMA, in order to obtain the beta beating functions and the phase advance in both vertical and horizontal planes. Figures 5.5 - 5.8 sketch those optics quantities. Similar behaviors can be matched with the experimental results, such as the tendency around zero of beta beating in both the horizontal and vertical planes. Not the same case for the phase advance, in which both planes present high fluctuations with large errors, in contrast with the experimental data. In chapter 4 some large errors are related to bad BPMs, in this case, the off tendency points cannot be associated to faulty BPMs as the tracking software do not set a random number of bad BPM signals, all of them work well.

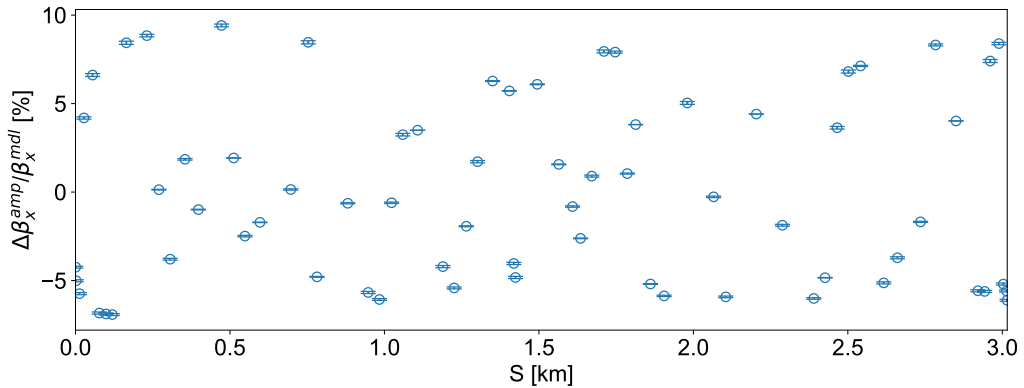


Figure 5.5: Horizontal Beta-beating function vs BPM longitudinal position in the HER obtained by SOMA code and simulation data.

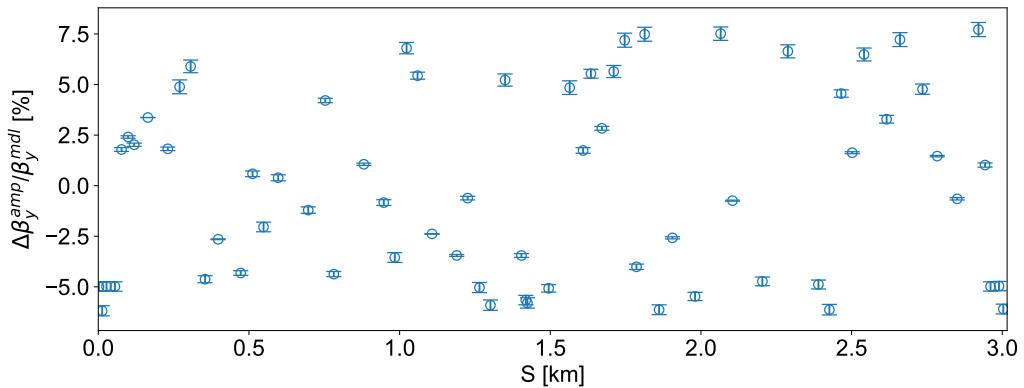


Figure 5.6: Vertical Beta-beating function vs BPM longitudinal position in the HER obtained by SOMA code and simulation data.

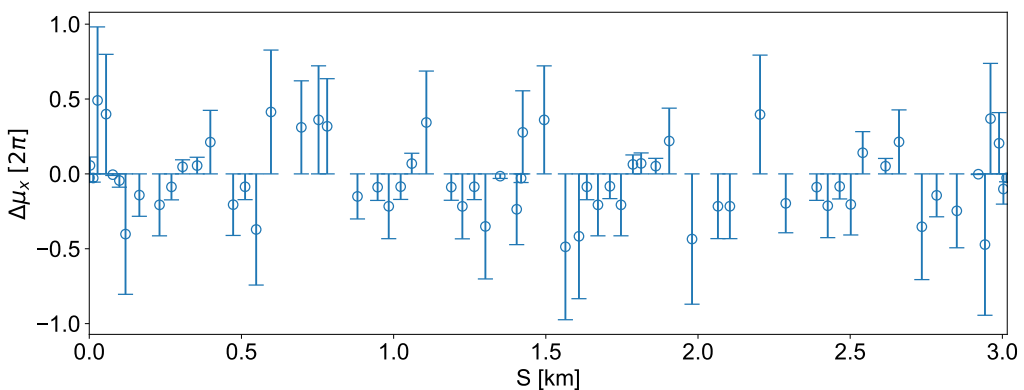


Figure 5.7: Horizontal Phase advance function vs BPM longitudinal position in the HER obtained by SOMA code and simulation data.

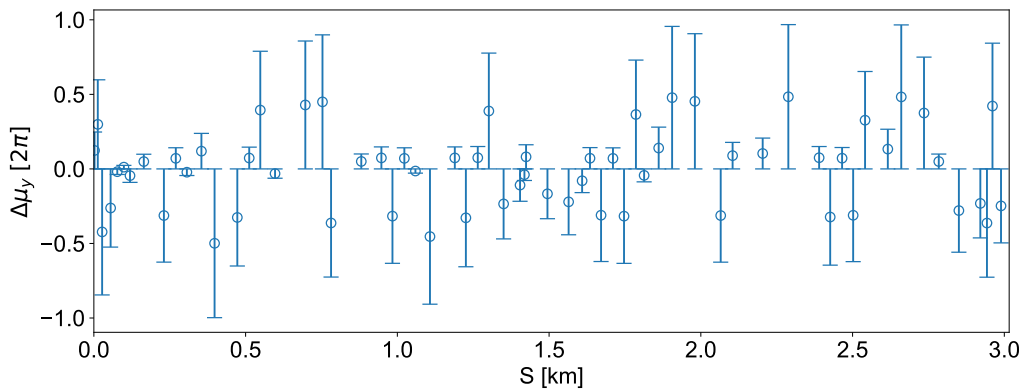


Figure 5.8: Vertical Phase advance function vs BPM longitudinal position in the HER obtained by SOMA code and simulation data.

### 5.3.1. RDTs

Employing SOMA method to obtain the RDTs, keeping into account the contribution of several measurements, the following figures display the complex amplitude of RDTs corresponding to Normal and Skew octupolar fields along the ring. From those simulations, is clear a large contribution of skew and normal octupole fields in the first mid section of the ring, for the vertical plane  $y$ , while contributions at the end of the pipe are covered by skew and normal octupole fields in the horizontal plane  $x$ .

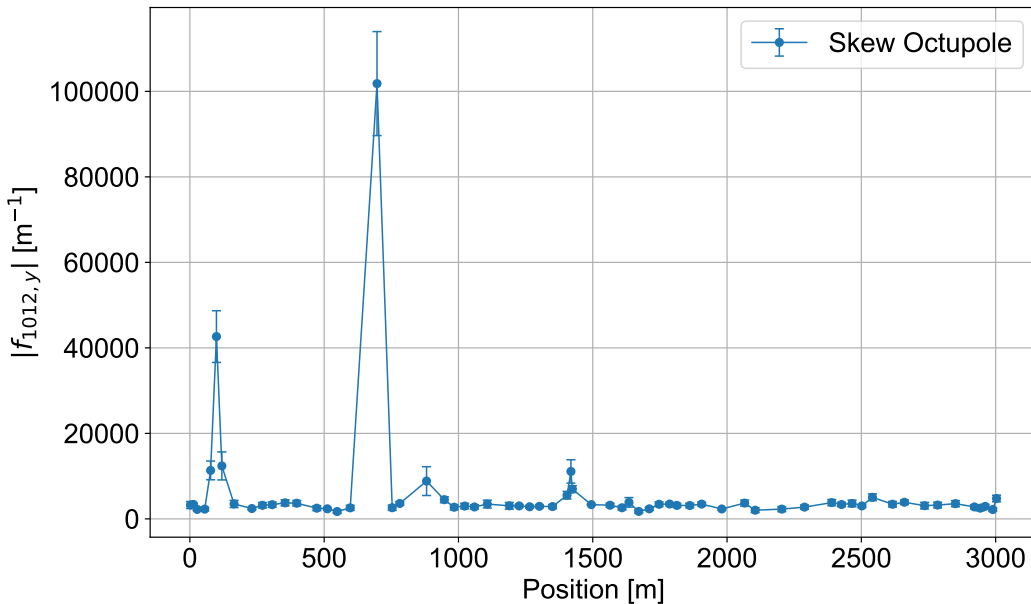


Figure 5.9: Skew Octupolar RDT  $f_{1012}$  obtained from tracking in HER for the vertical plane.

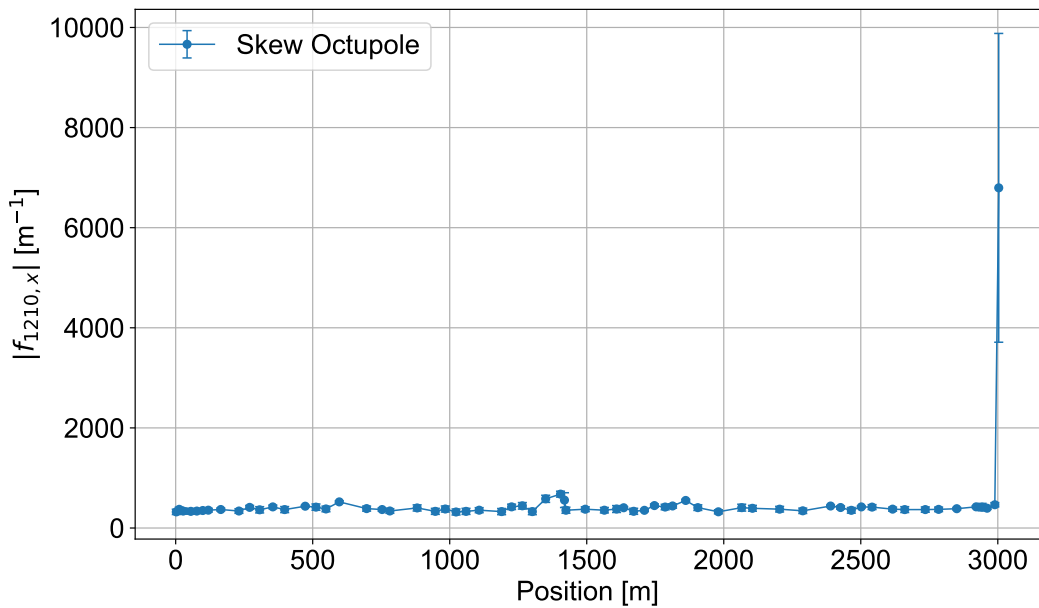


Figure 5.10: Skew Octupolar RDT  $f_{1210}$  obtained from tracking in HER for the horizontal plane.

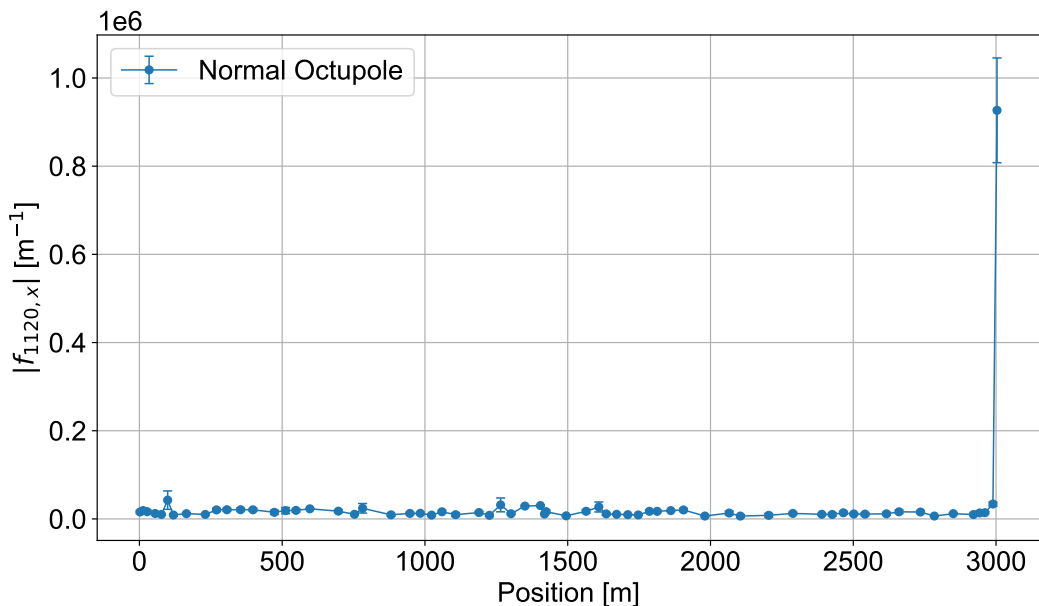


Figure 5.11: Normal Octupolar RDT  $f_{1120}$  obtained from tracking in HER for the horizontal plane.

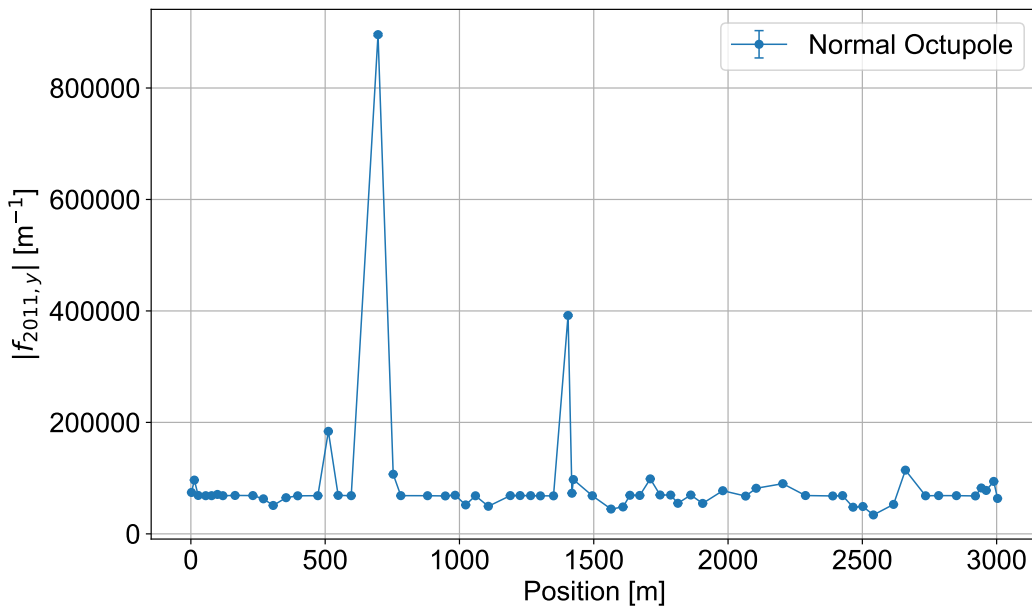


Figure 5.12: Normal Octupolar RDT  $f_{2011}$  obtained from tracking in HER for the vertical plane.

## 5.4. Cross validation

The main goal of the tracking is to check its validity over the experimental data for a given date, and then observe inconsistencies in the model. For the purpose of comparison between the experimental and simulation, it is required a scale to overlap both spectras. Employing a simple linear scale with respect to the main peak, majority of tracking and data do not show incoherence between them. Nevertheless, some of them such as the ones in Figures 5.13 and 5.14 sketch interesting irregularities to be studied along the full spectra. Special case in the vertical plane, where some resonances from the tracking data do not have a corresponding one in the experimental data, and similar in the opposite way. Similarly, Figures 5.16 to 5.18 displays the contrast between the normal and skew octupole RDTs studied in the last chapter.

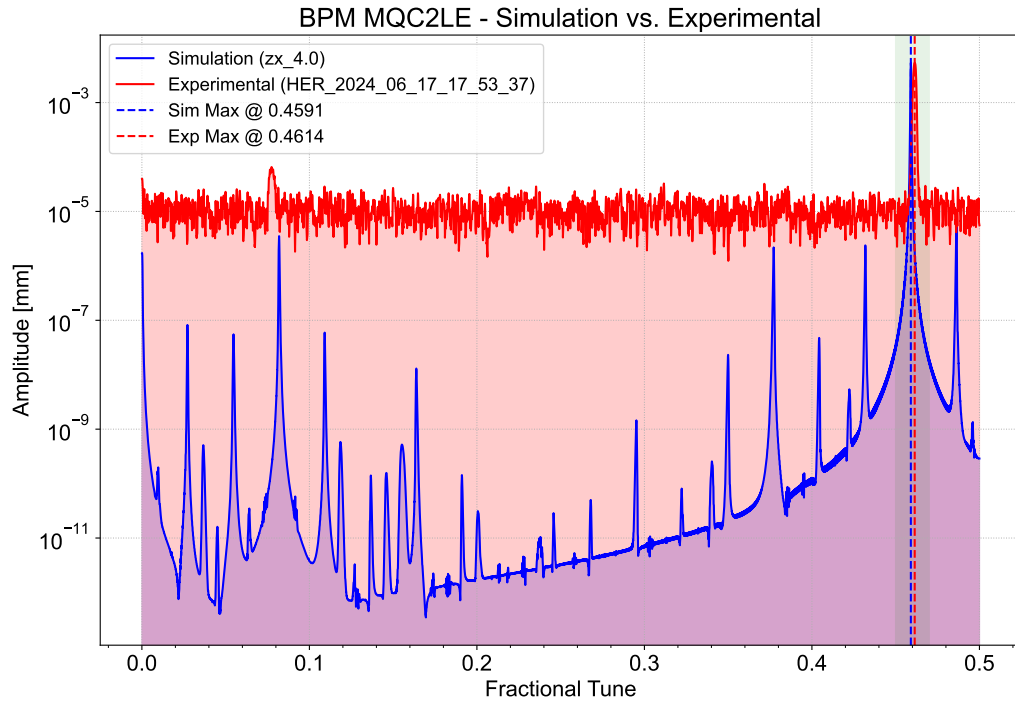


Figure 5.13: Contrast in the horizontal plane between the tracking vs experimental data with lattice of June 17 - 2024 in common. Action for simulation is set in 4.

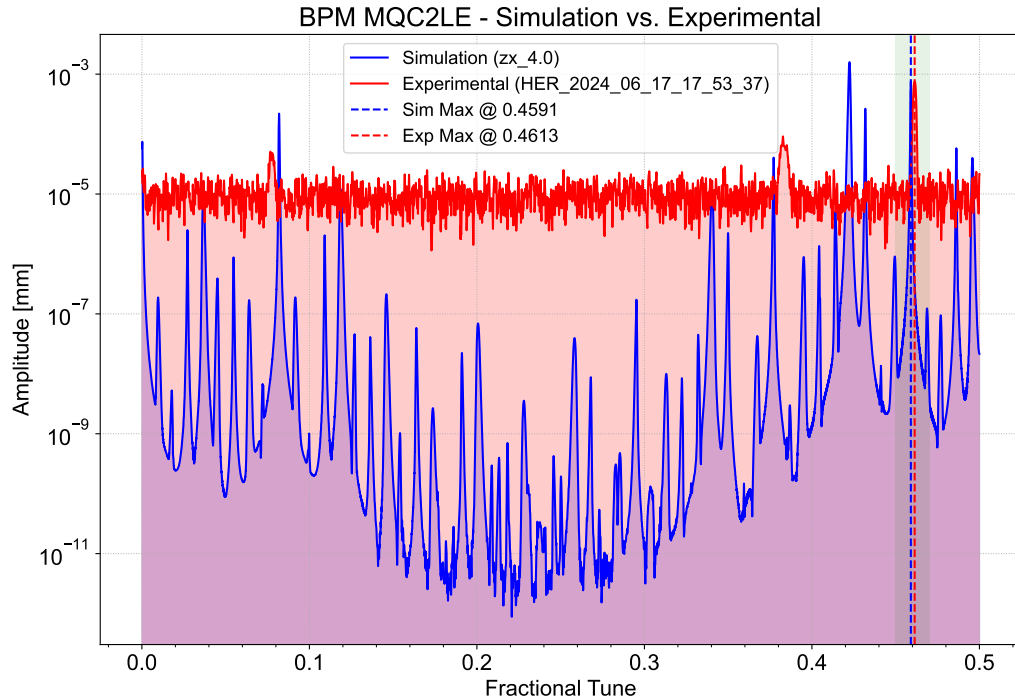


Figure 5.14: Contrast in the vertical plane between the tracking vs experimental data with lattice of June 17 - 2024 in common. Action for simulation is set in 4.

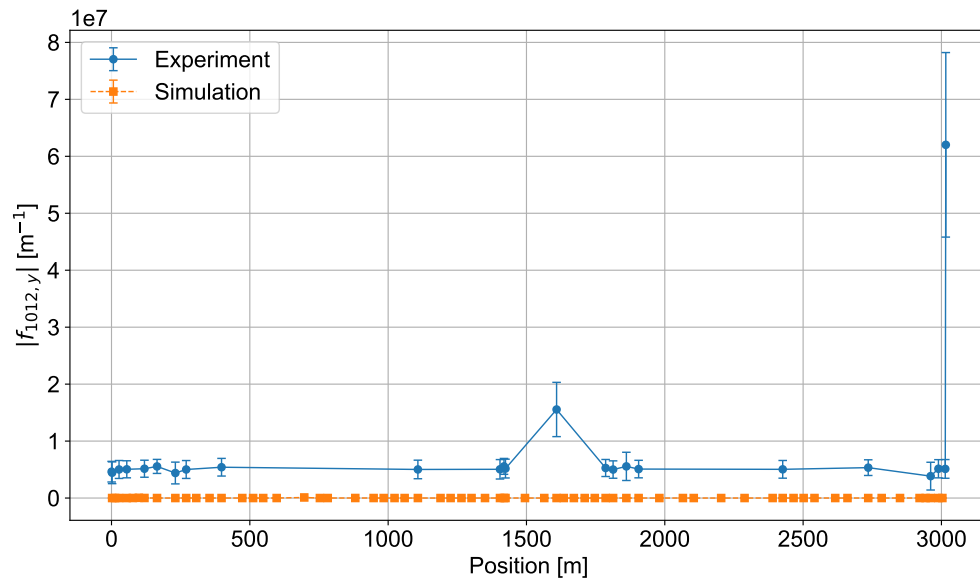


Figure 5.15: Contrast in the vertical plane between the tracking vs experimental skew octupolar RDT  $f_{1012}$  with lattice of June 17 - 2024 in common. Action for simulation is set in 4.

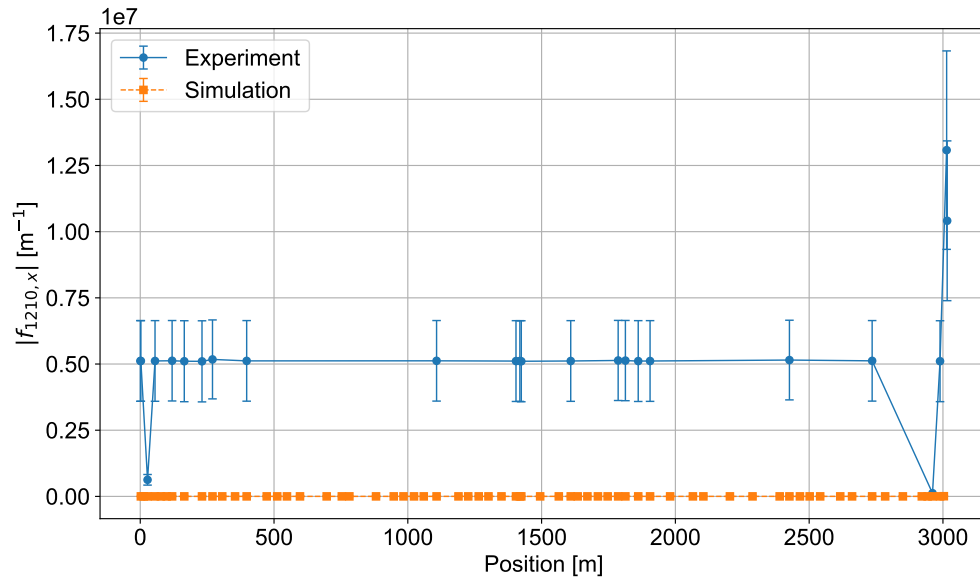


Figure 5.16: Contrast in the horizontal plane between the tracking vs experimental skew octupolar RDT  $f_{1210}$  with lattice of June 17 - 2024 in common. Action for simulation is set in 4.

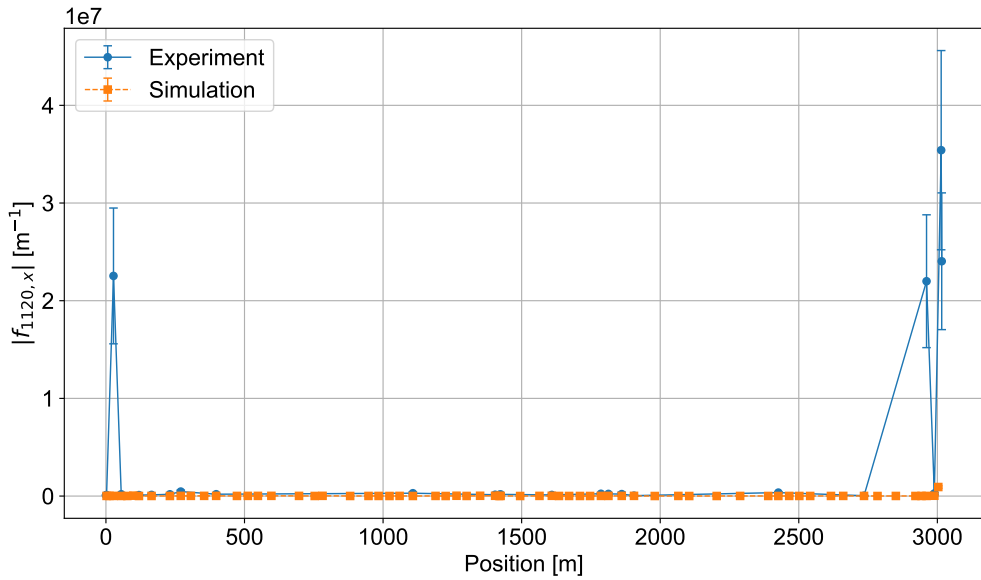


Figure 5.17: Contrast in the horizontal plane between the tracking vs experimental normal octupolar RDT  $f_{1120}$  with lattice of June 17 - 2024 in common. Action for simulation is set in 4.

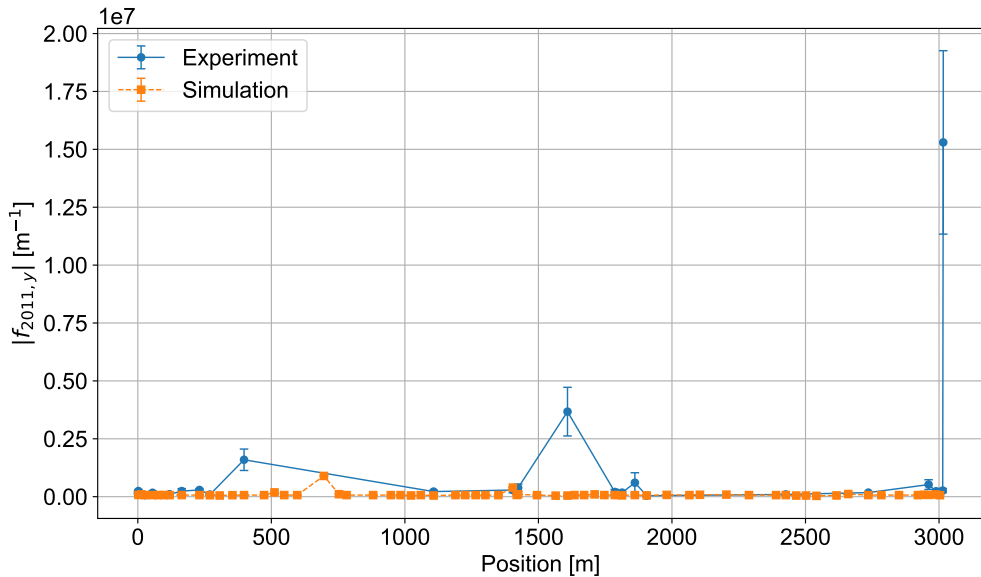


Figure 5.18: Contrast in the vertical plane between the tracking vs experimental normal octupolar RDT  $f_{2011}$  with lattice of June 17 - 2024 in common. Action for simulation is set in 4.

From these last plots, it is clear that skew contributions from the tracking are negligible compared to the experimental amplitudes, which could be consequence of high order fields that are not considered into the lattice file of the measurements. For the contrary, the normal

octupole field fits the background of experimental RDTs, but without showing any off measurement from the tendency, which could be the same problem as the skew case. In this point, it is important to remark that last simulations are chosen in order to appear similar to the real betatron oscillation from data, as it is difficult to know the exact parameters of the horizontal kick, to set as input of the simulations, this could bring errors that are not taken into account for this study.

---

# Conclusions

---

This work presented the analysis of Turn-by-Turn Beam Position Monitor (BPM) data from the SuperKEKB main rings, with the dual objectives of detecting anomalies, and extracting optics-related quantities using the SOMA framework, as well as benchmarking these results against tracking simulations. The study was motivated by the advances in the Optics Measurement and Corrections LHC team to identify and quantify higher-order nonlinear effects in the machine lattice, which can degrade beam quality and limit collider performance.

A theoretical background on beam dynamics and the Resonance Driving Terms (RDT) formalism was first reviewed, highlighting its capability to describe and classify nonlinearities through spectral analysis of BPM data. The SOMA package was then employed to process raw experimental Turn-by-Turn signals, applying denoising techniques such as Singular Value Decomposition (SVD), harmonic analysis for tune and spectral line identification, and optics reconstruction for beta-beating, phase advance, and RDT measurements.

Complementary tracking simulations, using the SuperKEKB software and lattice model, were performed to reproduce similar measurement conditions and excitation parameters. The same SOMA analysis pipeline was applied to the simulated data, enabling a direct comparison with experimental measurements. The results showed a general agreement between measured and simulated spectras and optics functions, as well as qualitative consistency in the extracted RDTs amplitudes and phases, although some discrepancies were observed, particularly with potential unmodeled octupolar-like sources, likely related to differences between the ideal lattice model and the real machine configuration.

Overall, this thesis demonstrated that LHC-developed analysis tools, such as OMC3, can be successfully adapted to the SuperKEKB context, providing a robust framework for the extrac-

tion of nonlinear optics parameters from Turn-by-Turn BPM data. The sequential methodology allowed for an efficient processing of signals, the identification of key spectral features, and the quantification of multipolar effects through RDT measurements.

The outcomes of this work contribute to the ongoing effort to refine beam-based diagnostics and correction strategies at SuperKEKB. They also establish a basis for future developments, including the incorporation of more realistic lattice models, improved synchronization across BPMs, and extended measurements under varied operational conditions. Such advancements will be essential for further optimization of the machine’s performance and for informing the design and operation of future high-luminosity circular colliders.

---

# Appendices

---

## A. BPM features

This appendix summarize general information of the whole BPM system at the main rings of SuperKEKB. Table A.1 presents technical features for different types of BPMs, from them the Gated Turn-by-Turn are used for the measurements analyzed in this work. Tables A.2 and A.3 present the list of Turn-by-Turn BPMs as well as its position in both HER and LER rings.

Type	Function	Resolution	Repetition	Number of units	
1GHz Narrow-band system from KEKB	Closed orbit correction, CCC, optics measurement	$3\mu\text{m}$	0.25Hz	109	
New narrow-band with 509MHz detection	As above	2 to $3\mu\text{m}$	0.25Hz	133	
Gated Turn-by-Turn	Injection tuning, optics measurement	$50 - 100\mu\text{m}$	100kHz/data	117	
Medium-band (Libera)	Measurement of orbit variation	< 2 to $3\mu\text{m}$	10kHz	4	
Fast orbit deviation (Libera)	Orbit deviation abort	$\sim 10\mu\text{m}$	$< 10$ turn	100kHz	4

Table A.1: Technical description of the BPM diagnostic system at SuperKEKB collider [7].

HER		LER	
BPM	Position (m)	BPM	Position (m)
MQC1LE	0.5300002	MQC1LP	0.5100004
MQC2LE	2.2500008	MQC2LP	2.2500020
MLQC3LE	12.9355133	MLQC2LP	21.1251386
MLQC7LE	27.2720861	MLQC3LP	28.6858930
MQLB1LE	55.2235731	MQLB1LP	67.0736866
MQLB4LE	77.1787307	MQLB4LP	94.3815635
MQLA2LE	98.9121927	MQLA2LP	119.6907156
MQLA5LE	119.0986538	MQLA5LP	140.2135966
MQD3E1	164.5639584	MQEAP3	204.8643915
MQEAE4	230.8020191	MQD3P3	239.1891319
MQD3E4	270.0136808	MQEAP6	305.0773528
MQEAE6	306.4724249	MQTATNP1	357.0045303
MQTATNE1	354.4092937	MQTATNP2	397.2161569
MQTATNE2	397.7476034	MQEAP8	473.2115007
MQEAE8	472.7108711	MQD3P8	515.0315554
MQD3E8	511.9225329	MQEAP10	549.3562958
MQEAE10	548.3812769	MQEAP11	601.4329246
MQEAE11	597.0252838	MQS1NP1	639.5156159
MQR2NE1	696.7698054	MQFWNP2	736.1192362
MQFRNE3	753.3246054	MQDWNP5	783.2482362
MQDRNE5	781.6020054	MQS2NP2	879.4059116
MQEAE13	881.1975280	MQD3P11	917.9653219
MQD3E12	947.4355886	MQEAP16	983.8535428
MQEAE16	983.8943327	MQD3P14	1025.6735975
MQD3E14	1023.1059944	MQEAP18	1059.9983379
MQEAE18	1059.5647385	MQTANFP1	1111.9255154
MQTANFE1	1107.5016074	MQD3P16	1193.8077453
MQD3E16	1189.3444407	MQEAP20	1228.1324858
MQEAE20	1225.8031848	MQD3P18	1269.9525404
MQD3E18	1265.0148465	MQEAP22	1304.2772808
MQEAE22	1301.4735906	MQD3P20	1346.0973355
MQEAE23	1350.1175975	MQEAP24	1380.4220759
MQI6E	1404.3012987	MQR5P	1409.8541059
MQI5E	1418.7440064	MQV4P1	1485.7111905
MQI4E	1424.1361014	MQV1P2	1520.7176968

Table A.2: BPM list for Turn-by-Turn measurements in the first half of HER and LER rings.

HER		LER	
BPM	Position (m)	BPM	Position (m)
MQX2RE	1494.6206604	MQI6P	1601.3758856
MQM2E	1564.3492168	MQI7P	1611.0743145
MQM7E	1608.8759522	MQI8P	1617.1601171
MQEAE25	1634.7988225	MQEAP25	1638.0874823
MQD3E21	1671.2575666	MQD3P21	1672.4122228
MQEAE27	1710.4692283	MQEAP27	1714.2322774
MQD3E23	1746.9279724	MQD3P23	1748.5570178
MQEAE29	1786.1396341	MQEAP29	1790.3770725
MQEAE30	1813.1660330	MQEAP30	1814.4452387
MQTAFOE1	1861.1278611	MQTAFOP1	1866.5350062
MQTAFOE2	1905.3942301	MQTAFOP2	1905.5101830
MQEAE32	1980.3824571	MQEAP32	1981.6681167
MQD3E29	2065.4852081	MQEAP33	2033.7447456
MQEAE35	2104.6968698	MQD3P29	2068.0694860
MQR2ORE	2203.8099939	MQEAP35	2109.8895407
MQDROE5	2288.3421939	MQW2ORP	2206.4670173
MQEAE37	2389.8065079	MQFWOP3	2262.9718173
MQD3E31	2426.2652520	MQS2OP2	2386.9512578
MQEAE39	2465.4769137	MQEAP38	2415.2540939
MQD3E33	2501.9356578	MQEAP39	2467.3307228
MQEAE41	2541.1473195	MQD3P33	2501.6554632
MQTAOTE1	2616.1355465	MQEAP41	2543.4755179
MQTAOTE2	2660.4019155	MQTAOTP1	2619.6334516
MQEAE44	2735.3901425	MQTAOTP2	2658.6086284
MQEAE45	2784.0341494	MQEAP44	2734.7665621
MQD3E40	2850.2722100	MQD3P38	2776.5866168
MQLA2RE	2920.9780873	MQEAP46	2810.9113572
MQLB8RE	2942.8131119	MQLA5RP	2885.7820303
MQLB1RE	2960.9918734	MQLA2RP	2900.3824801
MQLC7RE	2989.1433603	MQLB4RP	2923.2915425
MQLC3RE	3003.3799331	MQLB1RP	2955.5304075
MQC2RE	3013.8146988	MQLC3RP	2989.2325719
MQC1RE	3015.7846995	MQLC2RP	2996.7933257
		MQC2RP	3013.8064969
		MQC1RP	3015.7964987

Table A.3: BPM list for Turn-by-Turn measurements in the second half of HER and LER rings.

## B. Amplitude, Resonances and Lines

This part follows the results in [9], and is focused on individual Resonance Driving Terms, detailing what type of magnet they originate from, what resonance they excite, how they can be observed, and what kick are needed in order to measure them. The color coding helps quickly identifying dependencies:

- $I_x$ : depends only on the normalized horizontal amplitude
- $I_y$ : depends only on the normalized vertical amplitude
- $I_x I_y$ : depends on both the normalized horizontal and vertical amplitudes

$n$	$jklm$	Type	Resonance	H-line	V-line	Amplitude H	Amplitude V
2	0020	normal	(0, 2)		(0, -1)		$4(2I_y)^{1/2}$
2	2000	normal	(2, 0)	(-1, 0)		$4(2I_x)^{1/2}$	
2	0110	skew	(-1, 1)		(1, 0)		$2(2I_x)^{1/2}$
2	1001	skew	(1, -1)	(0, 1)		$2(2I_y)^{1/2}$	
2	1010	skew	(1, 1)	(0, -1)	(-1, 0)	$2(2I_y)^{1/2}$	$2(2I_x)^{1/2}$

Table B.1: List of spectral lines driven by resonances and corresponding RDTs, for the quadrupole case.

$n$	$jklm$	Type	Resonance	H-line	V-line	Amplitude H	Amplitude V
3	0111	normal	(-1, 0)	(1, 1)			$2(2I_x)^{1/2}(2I_y)^{1/2}$
3	0120	normal	(-1, 2)	(1, -1)			$4(2I_x)^{1/2}(2I_y)^{1/2}$
3	1002	normal	(1, -2)	(0, 2)		$2(2I_y)$	
3	1011	normal	(1, 0)	(0, 0)	(-1, 1)	$2(2I_y)$	$2(2I_x)^{1/2}(2I_y)^{1/2}$
3	1020	normal	(1, 2)	(0, -2)	(-1, -1)	$2(2I_y)$	$4(2I_x)^{1/2}(2I_y)^{1/2}$
3	1200	normal	(-1, 0)	(2, 0)		$2(2I_x)$	
3	2100	normal	(1, 0)	(0, 0)		$4(2I_x)$	
3	3000	normal	(3, 0)	(-2, 0)		$6(2I_x)$	
3	0012	skew	(0, -1)	(0, 2)			$2(2I_y)$
3	0021	skew	(0, 1)	(0, 0)			$4(2I_y)$
3	0030	skew	(0, 3)	(0, -2)			$6(2I_y)$
3	0210	skew	(-2, 1)	(2, 0)			$2(2I_x)$
3	1101	skew	(0, -1)	(1, 1)		$2(2I_x)^{1/2}(2I_y)^{1/2}$	
3	1110	skew	(0, 1)	(1, -1)	(0, 0)	$2(2I_x)^{1/2}(2I_y)^{1/2}$	$2(2I_x)$
3	2001	skew	(2, -1)	(-1, 1)		$4(2I_x)^{1/2}(2I_y)^{1/2}$	
3	2010	skew	(2, 1)	(-1, -1)	(-2, 0)	$4(2I_x)^{1/2}(2I_y)^{1/2}$	$2(2I_x)$

Table B.2: List of spectral lines driven by resonances and corresponding RDTs, for the sextupole case.

$n$	$jklm$	Type	Resonance	H-line	V-line	Amplitude H	Amplitude V
4	0013	normal	(0, -2)	(0, 3)			$2(2I_y)^{3/2}$
4	0031	normal	(0, 2)	(0, -1)			$6(2I_y)^{3/2}$
4	0040	normal	(0, 4)	(0, -3)			$8(2I_y)^{3/2}$
4	0211	normal	(-2, 0)	(2, 1)		$2(2I_x)(2I_y)^{1/2}$	$2(2I_x)(2I_y)^{1/2}$
4	0220	normal	(-2, 2)	(2, -1)		$4(2I_x)(2I_y)^{1/2}$	$4(2I_x)(2I_y)^{1/2}$
4	1102	normal	(0, -2)	(1, 2)		$2(2I_x)^{1/2}(2I_y)$	
4	1120	normal	(0, 2)	(1, -2)	(0, -1)	$2(2I_x)^{1/2}(2I_y)$	$4(2I_x)(2I_y)^{1/2}$
4	1300	normal	(-2, 0)	(3, 0)		$2(2I_x)^{3/2}$	
4	2002	normal	(2, -2)	(-1, 2)		$4(2I_x)^{1/2}(2I_y)$	
4	2011	normal	(2, 0)	(-1, 0)	(-2, 1)	$2(2I_x)^{1/2}(2I_y)$	$2(2I_x)(2I_y)^{1/2}$
4	2020	normal	(2, 2)	(1, -2)	(-2, -1)	$4(2I_x)^{1/2}(2I_y)$	$4(2I_x)(2I_y)^{1/2}$
4	3100	normal	(2, 0)	(-1, 0)		$6(2I_x)^{3/2}$	
4	4000	normal	(4, 0)	(-3, 0)		$8(2I_x)^{3/2}$	
4	0112	skew	(-1, -1)	(1, 2)		$2(2I_x)^{1/2}(2I_y)$	
4	0121	skew	(-1, 1)	(1, 0)		$4(2I_x)^{1/2}(2I_y)$	
4	0130	skew	(-1, 3)	(1, -2)		$6(2I_x)^{1/2}(2I_y)$	
4	0310	skew	(-3, 1)	(3, 0)		$2(2I_x)^{3/2}$	
4	1003	skew	(1, -3)	(0, 3)		$2(2I_y)^{3/2}$	
4	1012	skew	(1, -1)	(0, 1)	(-1, 2)	$2(2I_y)^{3/2}$	$2(2I_x)^{1/2}(2I_y)$
4	1021	skew	(1, 1)	(0, -1)	(-1, 0)	$2(2I_y)^{3/2}$	$4(2I_x)^{1/2}(2I_y)$
4	1030	skew	(1, 3)	(0, -3)	(-1, -2)	$2(2I_y)^{3/2}$	$6(2I_x)^{1/2}(2I_y)$
4	1201	skew	(-1, -1)	(2, 1)		$2(2I_x)(2I_y)^{1/2}$	
4	1210	skew	(-1, 1)	(2, -1)	(1, 0)	$2(2I_x)(2I_y)^{1/2}$	$2(2I_x)^{3/2}$
4	2101	skew	(1, -1)	(0, 1)		$4(2I_x)(2I_y)^{1/2}$	
4	2110	skew	(1, 1)	(0, -1)	(-1, 0)	$4(2I_x)(2I_y)^{1/2}$	$2(2I_x)^{3/2}$
4	3001	skew	(3, -1)	(-2, 1)		$6(2I_x)(2I_y)^{1/2}$	
4	3010	skew	(3, 1)	(-2, -1)	(-3, 0)	$6(2I_x)(2I_y)^{1/2}$	$2(2I_x)^{3/2}$

Table B.3: List of spectral lines driven by resonances and corresponding RDTs, for the octupole case.

## **C. Declaration of Originality**

I, **Andrés Gómez**, hereby declare that the thesis entitled "*Data analysis in Turn-by-Turn BPMs signals of SuperKEKB main rings*", submitted to **Université Paris-Saclay**, has been carried out by me under the supervision of **Francesca Bugiotti** and **Barbara Dalena**.

I affirm that this work is my own and has been written without any plagiarism. All sources of information used in this thesis have been duly acknowledged. This work has not been submitted, in whole or in part, for any other academic degree or qualification.

Place: \_\_\_\_\_

Date: \_\_\_\_\_

---

(Signature)

**Andrés Gómez**

---

# List of Figures

---

1.1	Schematic drawing of the accelerator complex at KEK [2]. . . . .	3
1.2	Layout of the SuperKEKB Main Ring (MR). One ring consists of four arc sections, four straight sections, and one collision point at Tsukuba (Belle II) [3]. . . . .	4
1.3	Schematic view of the BPM model used in SuperKEKB [6]. . . . .	5
1.4	BPM pickups used for HER (left) of 12 mm and for LER (right) of 6 mm [7]. . . . .	6
1.5	Image charges and BPM signals for a displaced beam bunch [4]. . . . .	6
1.6	The beam (bunch) intensity effect on the difference signal of a BPM pickup [4]. . . . .	7
1.7	Read-out (front-end) electronics for a BPM pickup [4]. . . . .	7
2.1	FODO cells, a basic cell composed of two drift spaces, a focusing and a defocusing quadrupole [9]. . . . .	10
2.2	Summary of relevant quantities in the phase-space ellipse $x'$ versus $x$ [10]. . . . .	14
3.1	A tilted dipolar magnetic field is seen as the sum of two orthogonal magnetic fields [10]. . . . .	16
3.2	An offset quadrupole is seen as a centered quadrupole plus a dipole [10]. . . . .	16
3.3	A tilted quadrupole is seen as a normal quadrupole plus another quadrupole tilted by 45° [10]. . . . .	16
3.4	Schematic view of a ring and its transfer maps, $M_w$ refer to sections free of nonlinearities, $H_w$ represent the nonlinear kicks [11]. . . . .	18
3.5	Tune diagram with resonance lines excited by different multipole orders. Resonances lines up to decapoles ( $n \leq 5$ ) for left and up to decatetrapole ( $n \leq 7$ ) for right [9]. . . . .	21

4.1	Beam position for the horizontal component, from some BPMs in the HER ring. Measurements taken on June 17 - 2024 at 17h 53m. . . . .	27
4.2	Beam position for the vertical component, from some BPMs in the HER ring. Measurements taken on June 17 - 2024 at 17h 53m. . . . .	28
4.3	Spectra in the Fourier Space of the fractional tune from BPM MQD3E1, for both transverse planes. Measurement taken from June 17 - 2024. . . . .	30
4.4	Map of the horizontal phase advance $\Delta\mu_x$ between all the BPMs in the HER ring, for all the measurements of June 17 - 2024. An important note this is before synchronization. . . . .	31
4.5	Map of the vertical phase advance $\Delta\mu_y$ between all the BPMs in the HER ring, for all the measurements of June 17 - 2024. An important note this is before synchronization. . . . .	31
4.6	Map of the horizontal phase advance $\Delta\mu_x$ between all the BPMs in the HER ring, for all the measurements of June 17 - 2024. This case is after synchronization. . . . .	32
4.7	Map of the vertical phase advance $\Delta\mu_y$ between all the BPMs in the HER ring, for all the measurements of June 17 - 2024. This case is after synchronization. . . . .	33
4.8	Fractional tune of some BPMs in the HER ring from measurements taken in June 17 - 2024. Amplitudes corresponding to the horizontal component. . . . .	34
4.9	Fractional tune of some BPMs in the HER ring from measurements taken in June 17 - 2024. Amplitudes corresponding to the vertical component. . . . .	34
4.10	Horizontal Beta-beating function vs BPM longitudinal position in the HER obtained by SOMA code. . . . .	35
4.11	Vertical Beta-beating function vs BPM longitudinal position in the HER obtained by SOMA code. . . . .	36
4.12	Horizontal Phase advance function vs BPM longitudinal position in the HER obtained by SOMA code. . . . .	36
4.13	Vertical Phase advance function vs BPM longitudinal position in the HER obtained by SOMA code. . . . .	36
4.14	Skew Octupolar RDT $f_{1012}$ measured in HER for the vertical plane. . . . .	37
4.15	Skew Octupolar RDT $f_{1210}$ measured in HER for the horizontal plane. . . . .	38
4.16	Normal Octupolar RDT $f_{1120}$ measured in HER for the horizontal plane. . . . .	38
4.17	Normal Octupolar RDT $f_{2011}$ measured in HER for the vertical plane. . . . .	39
5.1	Tracking beam position in the horizontal component, for some BPMs in the HER ring. Lattice used is from June 17 - 2024 at 17h 53m, and with action of 4. . . . .	42
5.2	Tracking beam position in the vertical component, for some BPMs in the HER ring. Lattice used is from June 17 - 2024 at 17h 53m, and with action of 4. . . . .	43

5.3	Fractional tune of some BPMs in the HER ring from simulation employing the lattice of June 17 - 2024. Amplitudes corresponding to the horizontal component and an action of 4. . . . .	44
5.4	Fractional tune of some BPMs in the HER ring from simulation employing the lattice of June 17 - 2024. Amplitudes corresponding to the vertical component and an action of 4. . . . .	45
5.5	Horizontal Beta-beating function vs BPM longitudinal position in the HER obtained by SOMA code and simulation data. . . . .	46
5.6	Vertical Beta-beating function vs BPM longitudinal position in the HER obtained by SOMA code and simulation data. . . . .	46
5.7	Horizontal Phase advance function vs BPM longitudinal position in the HER obtained by SOMA code and simulation data. . . . .	46
5.8	Vertical Phase advance function vs BPM longitudinal position in the HER obtained by SOMA code and simulation data. . . . .	47
5.9	Skew Octupolar RDT $f_{1012}$ obtained from tracking in HER for the vertical plane. . . . .	47
5.10	Skew Octupolar RDT $f_{1210}$ obtained from tracking in HER for the horizontal plane. . . . .	48
5.11	Normal Octupolar RDT $f_{1120}$ obtained from tracking in HER for the horizontal plane. . . . .	48
5.12	Normal Octupolar RDT $f_{2011}$ obtained from tracking in HER for the vertical plane. . . . .	49
5.13	Contrast in the horizontal plane between the tracking vs experimental data with lattice of June 17 - 2024 in common. Action for simulation is set in 4. . . . .	50
5.14	Contrast in the vertical plane between the tracking vs experimental data with lattice of June 17 - 2024 in common. Action for simulation is set in 4. . . . .	50
5.15	Contrast in the vertical plane between the tracking vs experimental skew octupolar RDT $f_{1012}$ with lattice of June 17 - 2024 in common. Action for simulation is set in 4. . . . .	51
5.16	Contrast in the horizontal plane between the tracking vs experimental skew octupolar RDT $f_{1210}$ with lattice of June 17 - 2024 in common. Action for simulation is set in 4. . . . .	51
5.17	Contrast in the horizontal plane between the tracking vs experimental normal octupolar RDT $f_{1120}$ with lattice of June 17 - 2024 in common. Action for simulation is set in 4. . . . .	52
5.18	Contrast in the vertical plane between the tracking vs experimental normal octupolar RDT $f_{2011}$ with lattice of June 17 - 2024 in common. Action for simulation is set in 4. . . . .	52

---

# List of Tables

---

3.1	Selection of index relative to skew quadrupole, normal and skew sextupole. . . . .	24
3.2	Multipole classification by order, number of poles, and number of resonance driving terms (RDTs). . . . .	24
3.3	List of spectral lines driven by resonances and corresponding RDTs, for the quadrupole case. . . . .	25
4.1	Skew and normal octupolar RDTs of interest, their associated resonances and the frequency spectrum lines they contribute to. . . . .	40
A.1	Technical description of the BPM diagnostic system at SuperKEKB collider [7].	56
A.2	BPM list for Turn-by-Turn measurements in the first half of HER and LER rings.	57
A.3	BPM list for Turn-by-Turn measurements in the second half of HER and LER rings. . . . .	58
B.1	List of spectral lines driven by resonances and corresponding RDTs, for the quadrupole case. . . . .	59
B.2	List of spectral lines driven by resonances and corresponding RDTs, for the sextupole case. . . . .	60
B.3	List of spectral lines driven by resonances and corresponding RDTs, for the octupole case. . . . .	61

---

# Bibliography

---

- [1] Haruyo Koiso Kazunori Akai Kazuro Furukawa. “SuperKEKB Collider”. In: (2018). URL: <https://arxiv.org/abs/1809.01958>.
- [2] KEK. *Operation of the SuperKEKB accelerator restarted after upgrades*. 2024. URL: <https://www.kek.jp/en/topics/202402291200>.
- [3] T. Ishibashi Y. Suetsugu K. Shibata. “SuperKEKB vacuum system operation in the last 6 years operation”. In: *Physical Review Accelerators and Beams* (2023). URL: <https://journals.aps.org/prab/abstract/10.1103/PhysRevAccelBeams.26.013201>.
- [4] M. Wendt. “BPMSystems: A brief Introduction to Beam Position Monitoring”. In: (2020). URL: <https://arxiv.org/abs/2005.14081>.
- [5] R. Tomás J. Keintzel. “SuperKEKB Optics measurements using Turn-by-Turn Beam Position Data”. In: (2021). URL: <https://cds.cern.ch/record/2807279?ln=en>.
- [6] Yukiyoshi Ohnishi Hiroshi Sugimoto. “Optics measurements at SuperKEKB using beam based calibration for BPM and BBA”. In: *JACoW* (2019).
- [7] Makoto Tobiyama. “The Beam Diagnostics of SuperKEKB rings”. In: *FTCF2024*. 2024.
- [8] P. Castro-Garcia. “Luminosity and beta function measurement at the electron-positron collider ring LEP”. PhD thesis. CERN, 1996. URL: <https://cds.cern.ch/record/316609/holdings?ln=pl>.
- [9] Mael Le Garrec. “LHC Effective Model For Optics Corrections”. PhD thesis. CERN, 2024. URL: <https://repository.cern/records/wtztf-mv419>.

- [10] *Imperfections and corrections*. CERN–Accelerator–School course on Numerical Methods for Analysis, Design and Modelling of Particle Accelerators, 2020. URL: <https://cds.cern.ch/record/2923746>.
- [11] Andrea Franchi. “Studies and Measurements of Linear Coupling and Nonlinearities in Hadron Circular Accelerators”. PhD thesis. Johann Wolfgang Goethe-Universität, 2006. URL: <https://publikationen.ub.uni-frankfurt.de/frontdoor/index/index/docId/2270>.
- [12] LHC. *Welcome to omc3’s documentation!* 2025. URL: <https://pylhc.github.io/omc3/>.
- [13] KEK. *SAD Home Page*. 2025. URL: <https://acc-physics.kek.jp/SAD/>.